

THE FORMATION OF SILICON NANOPARTICLES ON SILICON-ON-INSULATOR
SUBSTRATE BY THERMAL ANNEALING

THESIS

Presented to the Graduate Council of
Texas State University-San Marcos
in Partial Fulfillment
of the Requirements

for the Degree

Master of SCIENCE

by

Benedict Anyamesem-Mensah, B.S.

San Marcos, Texas
May 2007

THE FORMATION OF SILICON NANOPARTICLES ON SILICON-ON-INSULATOR
SUBSTRATE BY THERMAL ANNEALING

Committee Members Approved:

Gregory F. Spencer, Chair

Heather C. Galloway

Wilhelmus J. Geerts

Approved by:

J. Michael Willoughby
Dean of the Graduate College

COPYRIGHT

by

Benedict Anyamesem-Mensah

2007

DEDICATION

For: My Mom, Margaret.

ACKNOWLEDGEMENTS

I would like to express my deepest gratitude to my wonderful mom, Margaret. Throughout the course of my graduate studies, she has been extremely supportive. Without her love and support, I never could have made it this far. I would also like to thank my wonderful fiancée, Akos, who inspires me to strive for success and who motivates me to attain my full potential. Furthermore I would like to thank the Mathis family and my uncles, Vincent and Richard, for their support throughout my life and my education.

Academically and professionally I owe a great debt of gratitude to Dr. Spencer, who took on the arduous task of becoming my research advisor. The knowledge I have gained from him is invaluable, and I feel privileged to have had the opportunity to work under his supervision. I also want to thank Dr. Galloway and Dr. Ir. Geerts for serving on my committee, I owe additional thanks to Dr. Bandyopadhyay for his immense contribution to my studies. Finally I would like to thank Rosa Cardenas of UT-Austin, Joel Dunn Jr., John Paul Spearman, Chris Lohn and William Gibson for all their assistance throughout this study and my stay at Texas State University-San Marcos.

This manuscript was submitted on April 12, 2007.

TABLE OF CONTENTS

	Page
ACKNOWLEDGEMENTS	v
LIST OF TABLES	viii
LIST OF FIGURES	ix
ABSTRACT	xi
 CHAPTER	
1 INTRODUCTION	1
2 PREVIOUS WORK AND INSTRUMENT DESCRIPTION	6
Previous Silicon Nanoparticle Synthesis Methods	6
Instrumentation and Methods used for this Project	12
Ion Beam Assisted Deposition.....	12
Oxford Applied Research RF 50 Ion Source	13
X-ray and Diffraction.....	17
X-ray Diffraction	18
Secondary Ion Mass Spectrometry	19
Static SIMS	20
Dynamic SIMS.....	22
Depth Profiling.....	22
Rapid Thermal Anneal	23
Atomic Force Microscopy	25

	Tapping Mode AFM	28
	Probe Tip Characterization	29
3	EXPERIMENTAL PROCEDURE	32
	Sample Substrates	32
	Silicon Deposited by Ion Beam Deposition.....	32
	X-ray Diffraction	35
	Rapid Thermal Annealer.....	37
	Atomic Force Microscopy	39
4	DATA AND ANALYSIS	40
	Layer Composition.....	40
	Depth Profiling.....	42
	Nanoparticle Size Distribution.....	45
	AFM Images	47
	Unannealed and Annealed SiO ₂ Control Samples	47
	AFM Analysis of the 6 nm Silicon Layer after Anneal	48
	AFM Analysis of the 15 nm Silicon Layer after Anneal ...	57
	Comparison of silicon layer thicknesses and anneal temperatures	65
5	CONCLUSIONS.....	66
	APPENDIX A – RTA Operation Procedure.....	69
	APPENDIX B – AFM Operation Procedure	70
	APPENDIX C – SIMS Measurements	77
	APPENDIX D – AFM Radius Measurements.....	78
	REFERENCES	81

LIST OF TABLES

		Page
Table 1:	DIBS Specification for the Ta/Si Deposition.....	34
Table 2:	DIBS Specifications for 60 second Si Deposition.....	34
Table 3:	DIBS Specifications for 30 second Si Deposition	34
Table 4:	Parameters of the AGTEST recipe	38
Table 5:	Color code of samples characterized by the x-ray diffractometer, with time and temperature of anneal.....	40
Table 6:	REFS computer data fit for Ta and Si.....	43

LIST OF FIGURES

	Page
Figure 1: Oxford Applied Research RF 50 Ion Source	14
Figure 2: A schematic diagram of the major processes in a gridded ion source together with their power supplies	15
Figure 3: Crystallographic planes reflecting x-rays	19
Figure 4: SIMS technique block diagram.....	21
Figure 5: AFM schematic	26
Figure 6: Interatomic forces versus distance curve	27
Figure 7: AFM scanning modes	29
Figure 8: DIBS ion source and vacuum chamber.....	35
Figure 9: Bede Scientific XRD instrument with the hood and the sample stage.....	37
Figure 10: The Total Fab Solution RTA System.....	38
Figure 11: Veeco AFM and Scanner Head	39
Figure 12: HAXRD scans for Ta and Si layers	41
Figure 13: REFS computer modeling for Ta and Si	42
Figure 14: A depth profile of a 30-second deposition of silicon on an SiO ₂ substrate ..	44
Figure 15: A depth profile of a 60-second deposition of silicon on an SiO ₂ substrate ..	44
Figure 16: Schematic of nanoparticle formation	46
Figure 17: AFM images for annealed and unannealed SiO ₂ samples.....	47
Figure 18: AFM images for the 6 nm Si on oxide sample annealed at 600°C	48

Figure 19:	AFM images for the 6 nm Si on oxide sample annealed at 650°C	49
Figure 20:	AFM images for the 6 nm Si on oxide sample annealed at 700°C	50
Figure 21:	AFM images for the 6 nm Si on oxide sample annealed at 750°C	51
Figure 22:	AFM images for the 6 nm Si on oxide sample annealed at 800°C	52
Figure 23:	AFM images for the 6 nm Si on oxide sample annealed at 850°C	53
Figure 24:	AFM images for the 6 nm Si on oxide sample annealed at 900°C	54
Figure 25:	Size distribution of the Si nanoparticles annealed at (a) 600°C, (b) 650°C, (c) 700°C and (d) 750°C.....	55
Figure 25:	Size distribution of the Si nanoparticles annealed at (e) 800°C, (f) 850°C and (g) 900°C.....	56
Figure 26:	A graph of temperature of anneal versus nanoparticle radius of silicon layer thickness of 6.0 nm	57
Figure 27:	AFM images for the 15 nm Si on oxide sample annealed at 600°C	58
Figure 28:	AFM images for the 15 nm Si on oxide sample annealed at 650°C	59
Figure 29:	AFM images for the 15 nm Si on oxide sample annealed at 700°C	60
Figure 30:	AFM images for the 15 nm Si on oxide sample annealed at 800°C	61
Figure 31:	AFM images for the 15 nm Si on oxide sample annealed at 850°C	61
Figure 32:	AFM images for the 15 nm Si on oxide sample annealed at 900°C	62
Figure 33:	Size distribution of the Si nanoparticles annealed at (a) 600°C, (b) 650°C, (c) 700°C and (d) 800°C.....	63
Figure 33:	Size distribution of the Si nanoparticles annealed at (e) 850°C and (f) 900°C.....	64
Figure 34:	A graph of temperature of anneal versus nanoparticle radius of silicon layer thickness of 15 nm	64
Figure 35:	A graph of temperature of anneal versus nanoparticle radius for both samples.....	65

ABSTRACT

THE FORMATION OF SILICON NANOPARTICLES ON SILICON-ON-INSULATOR SUBSTRATE BY THERMAL ANNEALING

by

Benedict Anyamesem-Mensah, B.S.

Texas State University-San Marcos

May 2007

SUPERVISING PROFESSOR: GREGORY F. SPENCER

In this study, we investigated the formation of silicon nanoparticles on a silicon-on-insulator (SOI) substrate that were created with a simple thermal treatment using temperatures ranging from 600°C to 900°C under atmospheric pressure in an inert gas (Ar). We studied the nanoparticle formation process versus the temperature of the thermal anneal, the thickness of the top silicon layer and we determined the variation of the particle size distribution with these parameters. The post-anneal substrate morphology is studied using *ex situ* atomic force microscopy (AFM). It was found that nanoparticle size increases with an increase in both the temperature and thickness of the top silicon layer. From a technological point of view, this study opens up a simpler way to synthesize silicon nanoparticles on an insulator.

CHAPTER 1

INTRODUCTION

Silicon has been widely recognized as the most important material of the 20th century. It is the second most abundant element in the Earth's crust, making up 25.7% of it by mass. Silicon does not occur isolated in nature: it mainly occurs in minerals consisting of (practically) pure silicon dioxide in different crystalline forms (quartz, chalcedony, opal) and as silicates (various minerals containing silicon, oxygen and one or another metal), for example feldspar. These minerals occur in clay, sand and various types of rocks like granite and sandstone. Silicon is the principal component of most semiconductor devices and, in the form of silica and silicates, in glass, cement, and ceramics. It is also a component of silicones. Silicon is widely used in semiconductors because it remains a semiconductor at higher temperatures than the semiconductor germanium and because its native oxide is easily grown in a furnace and forms a better semiconductor/dielectric interface than almost all other material combinations. These are the main reasons why Si became the fundamental component in integrated circuits and consequently in the microelectronic revolution.¹

From a chemical point of view, similar to other group IV elements, silicon easily forms four covalent bonds in tetragonal coordination (SP^3 hybridization) and typically crystallizes in a diamond-like structure. Unlike the case of carbon, which easily forms

strong π bonds through SP^2 hybridization (spanning an enormous variety of organic molecules and carbon materials, for example, graphite, fullerenes, nanotubes), the π bond in silicon compounds is rather weak ($\sim 25 \text{ kcal mol}^{-1}$ versus $\sim 60 \text{ kcal mol}^{-1}$ carbon) and reactive, so that only a few stable molecules with Si=Si double bonds (π -bonding) are known. Such a behavior, in turn, destabilizes the trigonal planar coordination, which promotes the crystallization of carbon into two-dimensional planar, tubular, and cage-like structures.²

The term nanoparticles refer to particles that have one or more dimensions on the order of nanometers (10^{-9} meters). Attention has recently been given to the nanoscale region as a new and exciting area of material science with numerous applications. Much research has been done to describe particles of this size. This task has proven challenging in that the nanometer size particles behave differently from their bulk-size counterparts. As the size of the particles decreases, the physical properties of the materials change dramatically. This arises from the fact that the size is now similar to physical quantities such as “grain size, magnetic domain size, elastic or inelastic scattering length of conduction electrons, wavelength of excitations such as phonons or magnons, De Broglie wavelength of the electron, phase-coherence length in a semiconductor, etc.”³

The desire to fabricate materials with novel or improved properties, which is driven by material science and technology, is currently giving the most significant contributions to nanoscale research. Such improved properties include strength, electrical and thermal conductivity, optical response, elasticity, or wear resistance. Research is also evolving toward materials that are designed to perform more complex and efficient tasks. Examples include materials that bring about a higher rate of decomposition of pollutants,

a selective and sensitive response toward a given biomolecule, and improved conversion of light into electric current or more efficient energy storage. For these and more complex tasks to be realized, novel materials have to be based on several components whose spatial organization is engineered at the molecular level.

In electronics, the design and the assembly of functional materials and devices based on nanoscale building blocks can be seen as the natural, inevitable evolution of the trend toward miniaturization. The microelectronics industry, for instance, is fabricating integrated circuits and storage media whose basic units are approaching the size of few tens of nanometers.⁴ Memory devices sensitive to the presence or absence of a single electron have the possibility to drastically improve device characteristics in terms of high density, low power usage, fast write/erase processes, and a long retention time. With the current scaling trends in metal-oxide-semiconductor field-effect transistors (MOSFETS), devices that operate with only a statistically small number of electrons and whose transport is mesoscopic are of potentially great importance. Silicon-based nanoscale devices are strong contenders in this future nanoelectronics technology due to the existing Si process infrastructure as well as the nearly perfect interface between the SiO₂ dielectric and Si. With crystals of 5 – 10 nm diameter, the Coulomb charging energy is significant and would form the basis for single-electron transistors as well as the self-limited charging of floating gate memory nodes.⁷

For computers, “smaller” means higher computational power at lower cost and with greater portability. However, this race toward higher performance is driving current silicon-based electronics to the limits of its capability. Fortunately, the advent of new methods for the controlled production of nano-scale materials has provided new tools that

can be adapted. New terms such as nanotubes, nanowires and quantum dots are now common jargon used throughout scientific publications. These objects are among the smallest man-made units that display physical and chemical properties which make them promising candidates as fundamental building blocks for novel transistors. The advantages envisioned here are higher device versatility, faster switching speed, lower power dissipation, and the possibility of packing many more transistors on a single chip.⁴

Substantial efforts have focused on investigating nanoscale forms of silicon, both for the purpose of further miniaturizing the current microelectronic devices and in the hope of unveiling new properties that often arise at the nanoscale. The trend in semiconductor device fabrication to miniaturize the size of microchips and their subcomponents with the idea that with smaller dimensions will come devices that will operate at faster speeds than preceding generations has led into the study of nanocrystalline silicon (nc-Si) devices for the development of quantum dots (QDs) compatible with large scale integration. These devices use nanocrystalline silicon materials where nanometer-scale crystalline silicon grains naturally form in large numbers from continuous films. The resulting silicon quantum dots are isolated from each other by thin oxide tunnel barriers formed at the silicon grain boundaries (GBs). The small grain size leads to large electron-confinement and single-electron charging energies, raising the possibility of room-temperature operation of QDs that display quantum size effects. The densely packed nature of the QDs is also of interest for quantum information processing in silicon.⁵

Silicon nanocrystals have a special interest for electronic and display applications because they are based on ordinary silicon that dominates microelectronics technology

today. These nanocrystals achieve their special properties by quantum confinement. In bulk silicon light emission requires phonon assistance due to the Si indirect gap, resulting in very low emission efficiency. As a result, bulk silicon photoluminescence is very weak or non-existent. In contrast, quantum confinement effects in silicon nanocrystals and porous silicon have been shown to enhance the luminescence efficiencies and quantum yield. This behavior is a result of the confinement of electron and hole wave functions similar to the classic quantum problem of a particle in a box. The result is quantized energy levels that depend on the size of the nanocrystallites. As the crystals become smaller and smaller, there is a transition from the bulk band structure to the quantized atomic energy structure whereby the gap is increased by decreasing the size of the crystal.⁶

The purpose of this research is to study the formation of silicon nanoparticles on a silicon-on-insulator (SOI) substrate by thermal annealing at atmospheric pressure (in an inert gas like Ar) and to determine how thickness of the original thin Si layer and temperature of annealing are related to the size of the nanoparticles that are formed.

The proceeding chapters discuss the study of the formation of the silicon nanoparticles by thermal annealing at atmospheric pressure. Chapter 2 describes the various methods that have been used to form these nanoparticles by other researchers and their results. Chapter 3 describes the experimental procedure used while the data are presented in chapter 4. The final chapter gives results, conclusions and suggestions for additional studies.

CHAPTER 2

PREVIOUS WORK AND INSTRUMENT DESCRIPTION

In this chapter, previous methods of silicon nanoparticle synthesis are reviewed. This will allow contrasting those methods with the method employed in this work. After this review, the critical instruments that were employed in this project will be described. Their operating principles will be briefly presented to understand how they were used in this project.

Previous Silicon Nanoparticle Synthesis Methods

A wide spectrum of synthesis methods are known to produce silicon nanocrystals. These methods include liquid phase and colloidal chemistry, gas phase processing, plasma processing, electron irradiation processing and thermal annealing processing.

The liquid phase processes are widely established for the production of silicon quantum dots. These methods include anodizing silicon wafers in a hydrofluoric acid solution, synthesis in inverse micelles, synthesis in high temperature supercritical solutions, the oxidation of metal silicides, the reduction of silicon tetrahalides and other alkylsilicon halides.⁸ Nayfeh et al.⁹ dispersed electrochemical etched silicon into a colloid of ultra bright blue luminescent nanoparticles and reconstituted it into films. With the film excited by a near-infrared two-photon process at 780 nm, the emission exhibited a sharp threshold near 10^6 W/cm², rising by many orders of magnitude. Under certain

conditions, spontaneous recrystallization forms crystals of smooth shape from which a collimated beam emission was observed, pointing to very large gain coefficient. The emission was in the blue (~400 nm) with a short time scale (10 ns). The particles were not heated or oxidized, Fourier transform infrared and electron photo spectroscopies showed that they were hydrogen terminated. In another study, Baldwin et al.¹⁰ reduced silicon tetrachloride with sodium naphthalenide in 1,2-dimethoxyethane at ambient temperature and pressure. This was followed by termination with n-buthyllithium, which gave rise to faceted tetrahedral silicon crystallites. The particles obtained had edge lengths between 40 and 130 nm with 95% of the particles falling within 40-80 nm range 80% falling within the 50-70 nm range.

Gas-phase processes are attractive for the synthesis of nanoparticles due to high processing rates that can be achieved through direct gas to particle conversion. A variety of gas-phase processes have been proposed to synthesize silicon nanocrystals. These include nanoparticle formation through high temperature thermal reactions (pyrolysis) of silane in furnace flow reactors, the decomposition of silane or disilane through laser light irradiation (photolysis) and laser pyrolysis using high power infrared lasers.

Silicon nanocrystals with diameters between 2.5 and 8 nm were prepared by Ledoux et al.¹¹ This was done by pulsed CO₂ laser pyrolysis of silane in a gas flow reactor where the flow was expanded through a conical nozzle into a high vacuum. Using a fast-spinning molecular-beam chopper, nanoparticles were selectively deposited by size on quartz substrates. The photoluminescence of the silicon nanocrystals and their yields were measured as a function of their size. It was found that the photoluminescence followed very closely the quantum-confinement model and the yield showed a

pronounced maximum for sizes between 3 and 4 nm. Batson et al.¹² used spatially resolved electron energy loss spectroscopy on single, hydrogen-terminated, to synthesis Si nanocrystals in the size range 2.5-50 nm. The particles were prepared via the gas-phase photolysis of a dilute Si₂H₆/He mixture in a gas flow cell (flows ~3-10 sccm), and deposited on a holey carbon grid for analysis. During particle synthesis, the pressure of the tube was maintained at 5 Torr. An ArF laser was directed down the entire axis of the flow cell, and was operated at 50 Hz and 300 mJ/pulse. The energy loss within a few eV of the core 2p ionization edge revealed information about the conduction band states. It was observed that the conduction band edge had shifted to higher energy as the inverse square of the particle radius. In addition, they found a strong increase in the oscillator strength for these transitions for decreasing particle sizes below 6 nm. Unfortunately, most gas phase processes suffer from rapid particle agglomeration due to the fact that particles are usually electrically neutral. For instance, Borsella et al.¹³ reported a particle size distribution with particle sizes ranging between 1-100 nm for their laser pyrolysis process. Agglomeration of nanoparticles is a severe problem, since it usually degrades the desired nanoparticle properties.

Nonthermal plasmas have been known for their ability to produce silicon nanoparticles for almost 20 years. However, these were generally considered from the viewpoint of a contamination problem in semiconductor processing and solar cell production. Hence the potential of using low-pressure plasmas for the high rate synthesis of silicon nanocrystals has so far remained widely underutilized. Several groups have demonstrated the synthesis of crystalline silicon nanoparticles with nonthermal plasmas. Oda et al.¹⁴ have developed a “digital plasma process”. In this process crystalline

particles were formed in a silane plasma produced in an ultra high frequency discharge and ejected from the plasma through injecting periodic pulses of hydrogen gas. In most of their work this group has focused on producing particles of less than 10-15 nm in size. Crystalline silicon and germanium particles were synthesized in a high-density helical resonator plasma by Gorla et al.¹⁵ Free-standing crystalline silicon particles of about 10 nm were also reported in the study of Viera et al.^{16, 17} In these studies, nanocrystals were produced in pulsed plasma using silane highly diluted in argon. It has to be emphasized that these plasma processes took place at low pressures of up to a few Torr.

In an effort to synthesize crystalline nanoparticles in a plasma using higher gas temperatures, Uwe Kortshagen et al. switched to a different system that operated at significantly higher power density.⁸ The base pressure prior to their plasma operation was 10^{-4} Torr in a discharge tube and 10^{-7} Torr in a high vacuum chamber. Their discharge was operated using a dilute mixture of 5% silane and 95% helium and argon, with a 2.5-sccm-silane : helium (5:95) flow and 3-sccm argon flow. This gave a discharge chamber pressure of 1500 mTorr. In this study, their development of the plasma process was capable of producing a relatively monodisperse, highly oriented nanoparticles 20-80 nm with a predominantly cubic shape.

In the formation of crystalline Si nanodots in SiO₂ films by electron irradiation, Du et al.¹⁸, transformed amorphous SiO₂ into crystalline Si by using 200kV electron irradiation at ambient temperature. The vacuum pressure in the specimen chamber of the UHV-TEM was less than 2×10^{-8} Pa. This transformation took place in two steps; the first step involved the transformation of amorphous SiO₂ into amorphous Si, while the second step was the crystallization of amorphous Si. The energy threshold for the

crystallization of amorphous Si was determined to be 150.2 kV. They concluded that the threshold energy in the formation of crystalline silicon can be achieved by combining lower energy electron (<150.2 kV) irradiation with heating the specimen to achieve a temperature above the crystallization temperature of silicon.

Seo et al.¹⁹ investigated the thermo-optic effect of Si nanocrystals in silicon-rich silicon oxide (SRSO) thin films with wavelength of 1530 nm. The SRSO thin films which consisted of nanocrystalline Si embedded inside a SiO₂ matrix, were prepared by electron-cyclotron-resonance plasma-enhanced chemical vapor deposition of SiH₄ and O₂ followed by a 30 min anneal at 1150°C. The refractive indices of all the SRSO films increased with increasing temperature, with the thermo-optic coefficient increasing from 1.0 to $6.6 \times 10^{-5} \text{ K}^{-1}$ as the Si content increased from 37% to 45%. It was concluded that, while the overall behavior can be understood as a mixture of the properties of Si and SiO₂, the thermo-optic coefficients of the nanocrystalline silicon displayed size-dependence consistent with the enlarged band gap of nanocrystal silicon. It was also speculated that thermo-optic effect might play a significant role during optical measurements of SRSO thin films.

A research into the formation of silicon islands on a silicon-on-insulator (SOI) substrate upon thermal annealing was undertaken by Legrand et al.²⁰ It was shown that a thermal treatment (in the 600-900°C range) induced the creation of silicon nanoparticles. The nanoparticle size and density were studied with an *ex situ* atomic force microscope. It was shown that the formation temperature of the nanoparticles increased from 575°C to 875°C as the initial silicon layer thickness increases from 1 to 19 nm. Their thermal

treatments were performed in an ultrahigh vacuum (UHV) chamber with a base pressure better than 2×10^{-10} Torr.

In the current work, we discuss the formation of silicon nanoparticles upon thermal annealing at atmospheric pressure in an inert gas. The silicon layer was formed by sputtering onto an oxidized substrate under vacuum with a base pressure of 3.0×10^{-7} Torr. This allowed a thin uniform silicon layer to be formed on the SiO_2 . The thermal treatments were done at an ambient pressure in argon gas. With temperatures ranging from 600°C to 900°C , we expected the creation of the silicon nanoparticles through this process.

Our process of the formation of nanoparticles has some similarities and differences with some of the methods discussed above. Most of the processes used an inert gas during their nanoparticles formations, some of the gasses discussed above include argon, helium and silane. This is in accordance with the type of gas we used in our process, argon gas was used in our thermal processes.

In the gas and plasma methods, the formation of the nanoparticles was done at very low pressures with some at UHV. As already mentioned, Batson et al. maintained a chamber pressure of 5 Torr during their particle synthesis and Uwe Kortshagen et al. used a discharge chamber of 1500 mTorr in their process whiles in our case, ambient pressure (760 Torr) is maintained in the RTA throughout the annealing. Even though Legrand et al. used thermal annealing process in their synthesis of the particles, they also maintained an ultrahigh vacuum with a base pressure of 10^{-10} Torr. One good reason for performing these treatments at atmospheric pressure is that UHV equipment is not required, making it less expensive to make these nanoparticles.

Instrumentation and Methods used for this Project

In these studies on the formation of crystalline silicon nanoparticles, the primary focus is to determine whether these particles could be formed on an SOI substrate by thermal annealing process at atmospheric pressure. In this section, the equipment and instrumentation used in the project are discussed. Their general methods of operation are described. The primary equipments used included a dual ion beam sputtering (DIBS) system, a secondary ion mass spectrometer (SIMS) system, x-ray diffraction (XRD) system, a rapid thermal annealer (RTA), and an atomic force microscope (AFM). The dual ion beam system was used to deposit the various thin films on the SiO₂-covered substrate. A secondary ion mass spectrometer was used to characterize the thickness of the various layers of films on the samples. These results were then compared to x-ray diffraction measurements. To anneal the samples to the required temperatures, a rapid thermal annealer was used. Finally the silicon nanoparticles were characterized by an atomic force microscope.

Ion Beam Assisted Deposition

Ion bombardment of biased substrates during sputtering is an effective way to modify film properties during the deposition. Process control in plasma is somewhat haphazard, however, because the direction, energy, and flux of the ions incident on the growing film are not usually well regulated. Ion-beam-assisted processes were invented to provide independent control of the deposition parameters and particularly, the characteristics of the ions bombarding the substrate. Two main ion source configurations are employed and these processes are:

- Dual-ion-beam system (DIBS)
- Ion-assisted deposition (IAD)

In the dual-ion-beam system, one source provides the inert or reactive ion beam to sputter a target in order to yield a flux of atoms for deposition onto the substrate.

Simultaneously, the second ion source, aimed at the substrate, supplies the inert or reactive ion beam that bombards the depositing film to tailor its properties.

In the second configuration, an ion source is used in conjunction with an evaporation source. The process, known as ion-assisted deposition, combines the benefits of high film deposition rate and ion bombardment. The energy flux and direction of the ion beam can be regulated independently of the evaporation flux.²¹ For the purpose of this study, the dual ion beam system was used to sputter the thin Si layer on top of SiO₂ coated Si substrates, forming the SOI samples.

Oxford Applied Research RF 50 Ion Source

The DIBS at the Physics Department of Texas State University–San Marcos uses an Oxford Applied Research RF 50 Ion Source as the primary ion beam for sputter deposition. It operates by means of an electrical discharge created through the inductive coupling of an RF excitation coil. The objective is to deliver all available power from a RF generator (with an operating frequency of 13.56 MHz) to the discharge tube with a minimum loss and without reflected power. Impedance mismatches at either end of the power transmission line result in a reflection of power. Standing wave voltages are avoided by matching the resistive impedance (load) of the cavity to the output resistance of the generator.

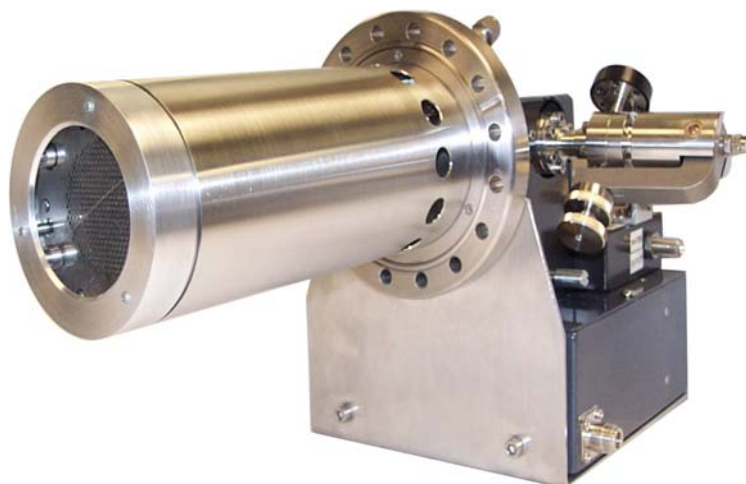


Fig. 1. Oxford Applied Research RF 50 Ion Source.

The ions, produced by dissociation in the RF discharge, are extracted into a vacuum with a grid set. The grid set consists of a screen and accelerator grid. The screen grid voltage defines the ion energy and is controlled by the high voltage power supply. The accelerator grid, held at a negative potential, is placed at a fixed distance from the screen grid. The electric field between these two grids extracts the ions from the plasma sheath and accelerates them to earth potential. There is a gas dependent critical pressure above which plasma ignition occurs, this occurs in the range of 10^{-4} Torr. Typical operational flow rates are between 10 and 20 standard cubic centimeters per minute (sccm). The grids have a very high transparency to achieve high ion current density.

There is a critical pressure above which breakdown of the gas will occur. The breakdown pressure of the gas will depend on its ionization potential. Consequently, for a fixed source conductance, the flow rate necessary to achieve breakdown will vary from gas to gas. Helium and hydrogen being light gases and of high ionization potential will require higher flow rates for breakdown than argon and nitrogen. Once breakdown has occurred, the flow rate can be turned down considerably while maintaining a discharge.

A cross section of a typical gridded ion source together with power supplies is presented in Figure 2. The ground indicated in the figure is the vacuum-chamber ground.

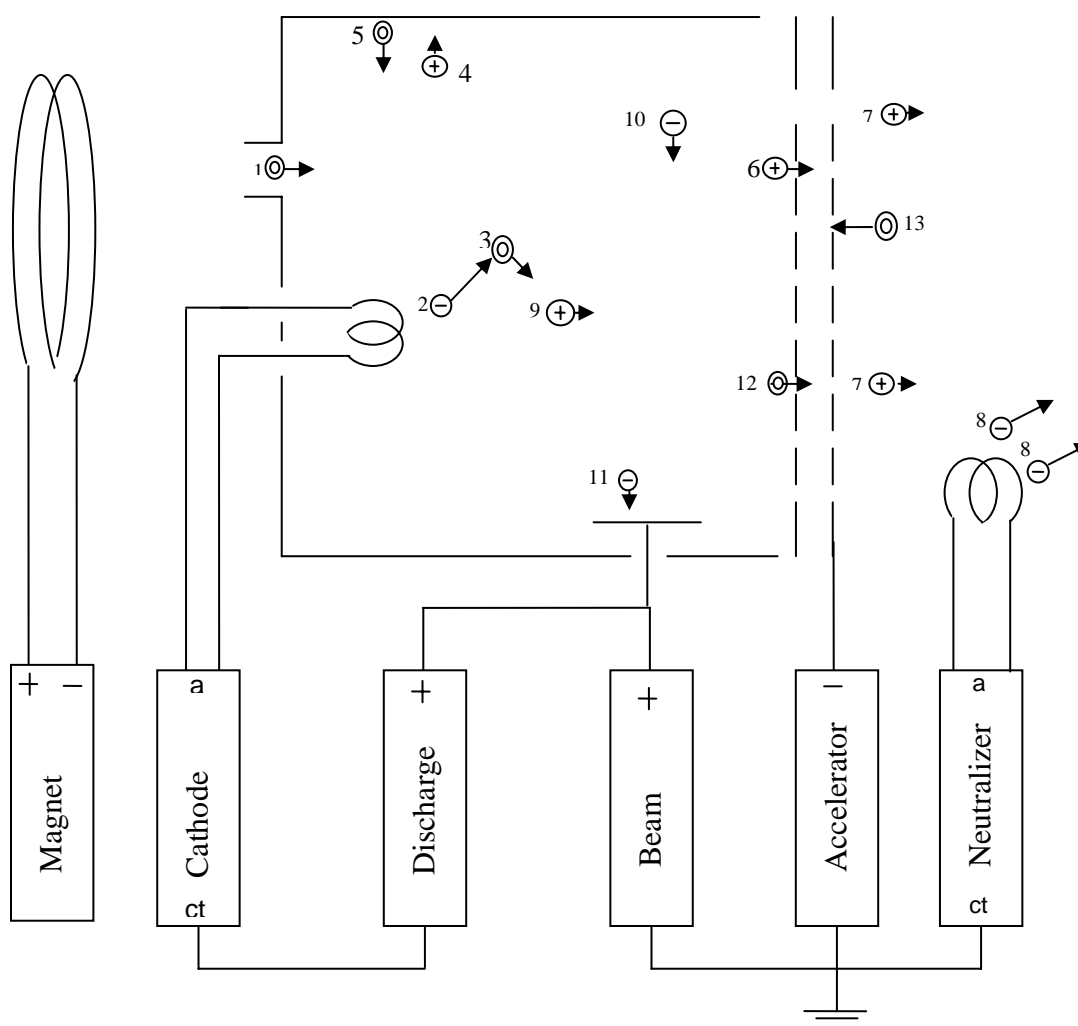


Fig. 2. A schematic diagram of the major processes in a gridded ion source together with their power supplies.

The neutral atoms or molecules (1) of the working gas are introduced into the discharge chamber through a port in the discharge-chamber wall. Argon is the most frequently used working gas. Energetic electrons (2) created by the RF excitation strike the atoms or molecules (3) within the discharge chamber. Some of the ions (4) produced by these collisions reach various surfaces within the discharge chamber and recombine with electrons at these surfaces. Some or all of the neutrals formed in this manner return

to the discharge-chamber volume (5). Other ions (6) are formed into small beamlets by passing through the apertures in the screen grid. The ions in these beamlets are attracted to the negative accelerator grid, but, in normal operation, pass through this grid without striking it, due to the alignment of the apertures in the two grids. The ion beam (7) is formed of the individual beamlets after they leave the accelerator grid. The ion beam is neutralized by electrons (8) from the neutralizer filament (or neutralizer cathode).

The energetic electrons (2), ions (9), and low-energy background electrons (10) in the discharge-chamber volume constitute an electrically conductive gas, or plasma. This plasma is nearly uniform in potential, typically varying only 1-5 V and only several volts higher than the anode potential. The anode is therefore the electrode that most closely approximates the origin potential for the ions.

The pressure within the discharge chamber is normally low enough that the mean path length between collisions for a gas atom or molecule is larger than the discharge-chamber dimensions. To increase the probability of ionization by an energetic electron (2) from the cathode before it escapes to the anode, a magnetic field is placed between the cathode and anode inside the discharge chamber.

Although the magnetic field is designed to be effective in containing energetic electrons (2), the low-energy background (10) can diffuse across the magnetic field relatively easily. The electron current inside the discharge chamber is therefore completed by low-energy electrons reaching the anode.

The low operating pressure also results in a gas backflow from the vacuum chamber into the discharge chamber. The gas flow is normally through the inlet port to the ion source, through the two grids into the surrounding vacuum chamber. Because the

path length between collisions is large, the outgoing atoms or molecules (12) seldom collide with the incoming atoms or molecules (13).²²

The vacuum chamber includes a substrate stage, target indexer to allow for changing sputter targets during deposition (without breaking vacuum), and an ARS. These are all cooled by a recirculator (maintaining 15°C during processing). The pumping system consist of a mechanical roughing pump (base pressure ~0.1 Torr), turbomolecular pump (base pressure $\sim 10^{-5}$ Torr), and a helium cryopump (base pressure $\sim 10^{-7}$ Torr). Pressures are monitored at various points around the system with a Bourdon gauge, a thermocouple gauge. There is also an SRS residual gas analyzer (RGA) to monitor and determine what gases are present in the system.

X-ray and Diffraction

X-rays are high-energy, short wavelength electromagnetic radiation. They have energies ranging from about 200 eV to 1 MeV, which puts them between γ -rays and ultraviolet (UV) radiation in the electromagnetic spectrum. X-rays are produced in an x-ray tube by collisions between an externally generated beam of electrons and the electrons in the shells of an atomic target, typically a Cu target. The x-rays given off by the target are characteristic of its electron shells and can be filtered to produce a nearly monochromatic x-ray beam. Diffraction, on the other hand, is a general characteristic of all waves which can be defined as the modification of the behavior of light or other waves by its interaction with an object.³⁴

When x-ray photons collide with electrons, some photons from the incident beam will be deflected away from the direction where they originally travel. If the wavelength of the scattered x-rays remain the same (i.e. the x-ray photon did not lose any energy), the

process is known as elastic scattering. These are the x-rays that are measured in experiments, as they contain information about the electron distribution of the material. Inelastic scattering occurs when the x-rays transfer some of their energy to the electrons.³⁵

X-ray Diffraction

X-ray diffraction (XRD) is a versatile, non-destructive technique that is used to determine the nature of different material structures and phases in a sample, based on their characteristic diffraction behavior under irradiation of a known x-ray wavelength. Each different structure or phase will only diffract an incident x-ray at a specific set of angles, which can be measured.³⁶

Diffracted waves from different atoms can interfere with each other and the resultant intensity distribution is strongly modulated by this interaction. If the atoms are arranged in a periodic fashion, as in crystals, the diffracted waves will consist of sharp interference maxima with the same symmetry as in the distribution of atoms. Measuring the diffraction pattern therefore allows us to deduce the distribution of atoms in a material.

The position of the peaks in an x-ray diffraction pattern are directly related to the interatomic separations in the crystal. In Figure 3 below, an incident x-ray beam interacts with the atoms arranged in a periodic manner.

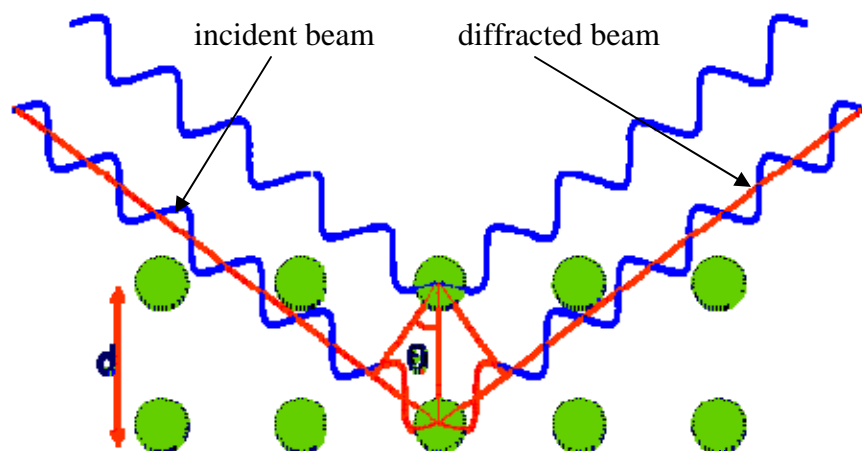


Fig. 3. Crystallographic planes reflecting x-rays.

For a given set of lattice plane with an inter-plane distance of d , the condition for a diffraction to occur is given by the relation

$$2d\sin\theta = n\lambda,$$

which is known as Bragg's law. Here λ is the wavelength of the x-ray, θ is the scattering angle, and n is an integer representing the order of the diffraction peak.³⁵

Secondary Ion Mass Spectrometry

Secondary ion mass spectrometry (SIMS) is a characterization method to determine the atomic and molecular species contained in a target material. It is based on the fact that charged atomic and molecular species are ejected from the surface of a condensed phase (liquid or solid) under heavy particle bombardment. These ejected species can be identified by mass spectrometry.

During this bombardment by ions or neutral particles, surface particles are sputtered and the primary bombarding particle is implanted into the condensed phase. The sputtering process results in two general groups of events:

- Changes in the bombarded surface.
- Emission processes.

The impact of a primary particle on a surface causes an energy and momentum transfer to a limited area around the point of particle impact, resulting in (1) a change of the lattice structure and (2) the loss of surface material by sputtering.

The ion-bombardment-induced emission processes include electron and photon emission and the emission of surface particles (atoms or molecules) in a charged or uncharged and possibly excited state. All these emission products are emitted with a certain angular distribution.

The secondary ion emission includes all emitted ionized surface particles in the ground state as well as in the excited state. These secondary ions may be easily mass separated by different types of mass analyzers (Figure 4). The secondary ion emission is the most powerful tool for the analysis of the uppermost monolayer of a solid: electron-mass ratio (e/m) spectrum of the secondary ions emitted from the bombarded surface supplies direct information on the chemical composition of the bombarded area. Erosion of the surface is caused when the atomic and molecular surfaces of the species are removed by the bombarding ions. Regarding this erosion process, two different modes of analytical SIMS application result.²³

Static SIMS

Static SIMS uses a pulsed primary ion beam to sputter material from the top monolayer of a sample. Secondary ions are collected and focused into a reflection time-of-flight (TOF) mass spectrometer, where they are separated according to mass. Mass separation is performed by measuring the length of time it takes secondary ions to reach the detector. The lighter the ion, the less time it takes to reach the detector. Highest mass

resolution is achieved by using the shortest primary ion pulses. The shorter the pulse, the more precise is the determination of the time it takes ions to reach the detector.

In Static SIMS, low doses of primary ions ensure that every secondary ion comes from an undisturbed region of the surface, allowing true surface analysis with SIMS sensitivities. It also performs mass analysis to determine the elemental and/or molecular composition of the top monolayer of a material's surface. Static SIMS can be used to analyze the masses of a wide range of organic and inorganic materials, including thin films, solid-state materials, ceramics, polymers, biological samples and catalyst particles. Imaging using a raster probe, static SIMS generates images to determine the lateral distribution of secondary ions.²⁴

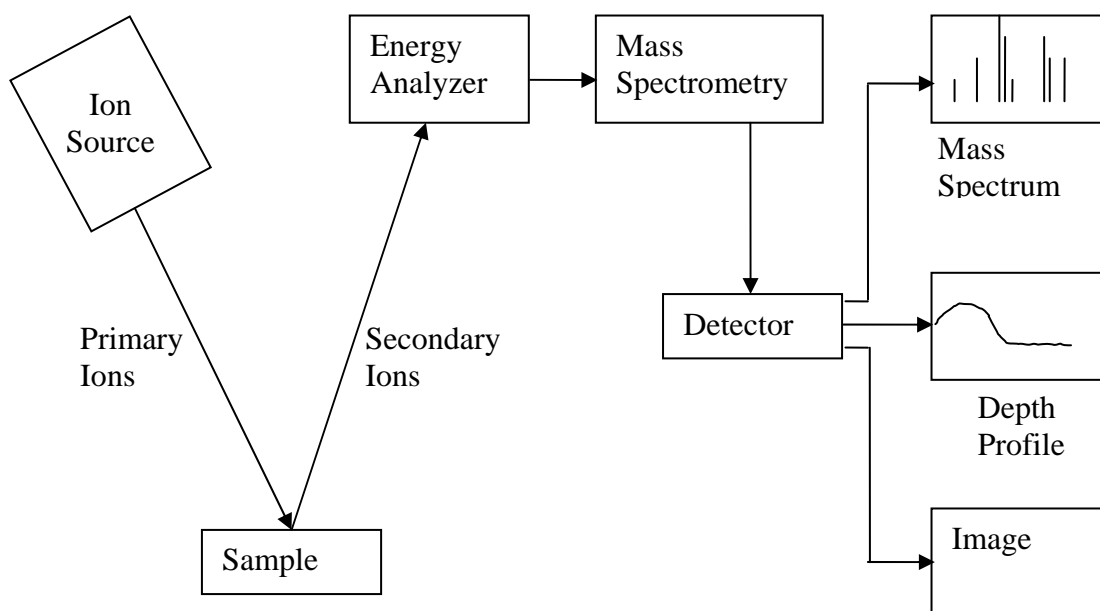


Fig. 4. SIMS technique block diagram.

Dynamic SIMS

With dynamic SIMS, the surface of a sample is bombarded with a continuous, focused beam of primary ions. The impact of the ions sputters (ejects) atoms from the surface of the material, producing secondary ions in the process. The secondary ions are extracted into a mass spectrometer, which uses electrostatic and magnetic fields to separate the ions according to their mass-to-charge ratio. Ions of different mass-to-charge ratios are measured by changing the strength of the magnetic field. Dynamic SIMS determines the elemental composition and the trace levels of impurities and dopants in solid materials.

By the use of dynamic SIMS, all the elements or isotopes in a material, from hydrogen to uranium can be identified. Elements, isotopes and compounds that have nominally identical atomic or molecular masses could also be differentiated. By sputtering into a material, dynamic SIMS can be used to determine the concentration of impurities or dopants as a function of depth (depth profiling). Dynamic SIMS is also capable of resolving dopant and impurity levels whose concentration is as much as nine orders of magnitude less than the atomic composition of the material.²⁵

In order to determine the thickness of the sputtered Si on the SiO₂, dynamic SIMS depth profiling was used confirm the thickness of each of the layers.

Depth Profiling

Depth profiles are obtained if, instead of scanning the mass spectrometer as the sputtering continues, one or more masses are monitored sequentially by switching rapidly among masses. The detected signal from the chosen species occurs from increasingly greater depths beneath the original sample surface.

Accurate depth profiling requires uniform bombardment of the analysis area and no contribution of ions from the crater walls, adjacent sample surfaces, or nearby instrument surfaces. In order to achieve good depth resolution, the sputtered area must be larger than the detected or analyzed area. Sputtered areas are defined by rastering the primary beam over a specific square or rectangular region. Continued sputtering over a rastered area produces a well-defined crater. The detected area is either located within the raster either by the use of an aperture or by electronic gating, so that the detection of secondary ions only occurs when the primary beam is in the gated area.

In a depth profile, the total rastered area cannot be used for detection of secondary ions because of contributions from the crater walls. The probability of nonuniform bombardment of the analysis area, which will reduce the depth resolution, increases as the analysis area is increased. Also, the sputtering rate decreases if the primary ion density is held constant while the rastered area is increased. Therefore, depth profiles should be obtained using different rastered and detected areas until a relationship between the ion beam raster and detected area can be established to avoid crater sidewall effects and optimize sputtering rate and depth resolution.²⁶

Rapid Thermal Anneal

Rapid thermal annealing (RTA) is a process used in semiconductor device fabrication which consists of heating a wafer in a short time in order to affect its electrical properties. The wafers are heated either by using lamp based heating, a hot chuck, or a hot plate. The Heatpulse 610 RTA was used to anneal the samples for a short period of time at precisely controlled temperatures. This short anneal helps decrease the time that the semiconductor substrate resides at high temperatures. This process helps decrease the

thermal budget (the integrated temperature-time product) of the substrate. This is needed in order to fabricate ever-small semiconductor transistors and other devices which are damaged by long high temperature treatments. In this project, the RTA was used to anneal the thin Si films to form the nanoparticles.

The wafer is sealed inside a quartz chamber where it is heated by 21 high-power tungsten halogen lamps. The sample temperature can be measured either with a thermocouple in thermal contact with the substrate holder or by pyrometer. The system has a gas-handling manifold so that various gases (O_2 , N_2 , Ar, N_2/H_2 etc) can flow into the anneal chamber before (for flushing), during (for processing), and after the annealing process (for clean cool-down). Different gas flows can be maintained to mix a combination of gases as well. In this project argon gas was circulated around the wafer during heating to prevent film oxidation in the heating cycles. Wafers are annealed using various process recipes that are stored in the RTA computer. Recipes include the time period for the temperature increase (the temperature ramp) and the duration and temperature of the thermal (the temperature soak) to properly anneal the wafer. This process can be used for standard annealing purpose (activating dopants, diffusion)³² or for more exotic processes like these nanoparticle studies.

The RTA has a lot of advantages over a conventional furnace. These include

- Closed-loop temperature control with pyrometer or thermocouple temperature sensing.
- Precise time-temperature profiler tailored to suit specific process requirements.
- Fast heating and cooling rates unobtainable in conventional technologies.
- Small footprint and energy efficiency.³³

Atomic Force Microscopy

Another instrument used to collect and process data for this study was an Atomic Force Microscope (AFM). The AFM is one of the Scanning Probe Microscopes (SPM) where a sharp probe is scanned across a surface and the probe/sample interaction is monitored.²³ The probe is a tip on the end of a cantilever which bends in response to the force between the tip and the sample.²⁶ The AFM works by measuring a local property, such as height, with the tip placed very close to the sample. To produce an image, the microscope scans the tip over the sample while measuring the property.²⁷

A simple schematic of an AFM instrument is shown in Figure 5 below. In this instrument the probe tip is mounted on the end of a triangular cantilever arm, similar to a diamond stylus mounted on the end of a record player arm. A piezoelectric device raster scans the sample beneath the probe tip. As the probe tip undergoes attractive or repulsive forces, the cantilever will bend. This bending of the cantilever can be monitored by bouncing a laser beam (a diode laser) off the cantilever onto a four element diode (Position Sensitive Photo Diode). In normal operation the tip-sample force is held constant by a computer controlled feedback loop that examines the force (bend of the cantilever) and tells the piezoelectric device whether to move the sample closer or farther away in order to maintain the set bending of the cantilever. The AFM image produced by taking the feedback signal at each pixel of the raster scan is mainly a measure of the topography of the sample.²⁸

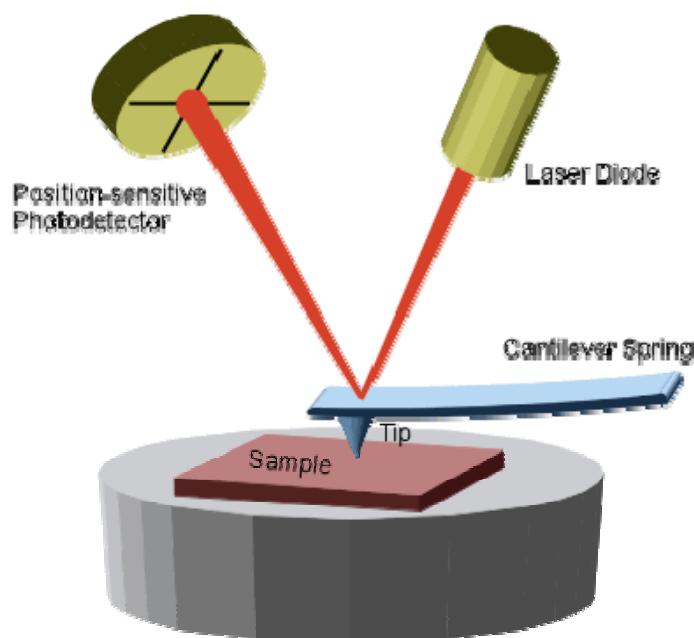


Fig. 5. AFM schematic.

Since the cantilever obeys Hooke's Law for small displacements, i.e. $F = -kx$ where:

- F = force
- k = spring constant
- x = cantilever deflection,

the interaction force between the tip and the sample can be found if the spring constant is known. The movement of the tip or sample is performed by an extremely precise positioning device made from piezo-electric ceramics, most often in the form of a tube scanner. The scanner is capable of sub-angstrom resolution in x-, y- and z-directions. The z-direction is conventionally perpendicular to the sample.³⁰

Several forces typically contribute to the deflection of an AFM cantilever. The force most commonly associated with atomic force microscopy is an interatomic force called the van der Waals force. The dependence of the van der Waals force upon the distance between the tip and sample is shown in Figure 6 below.

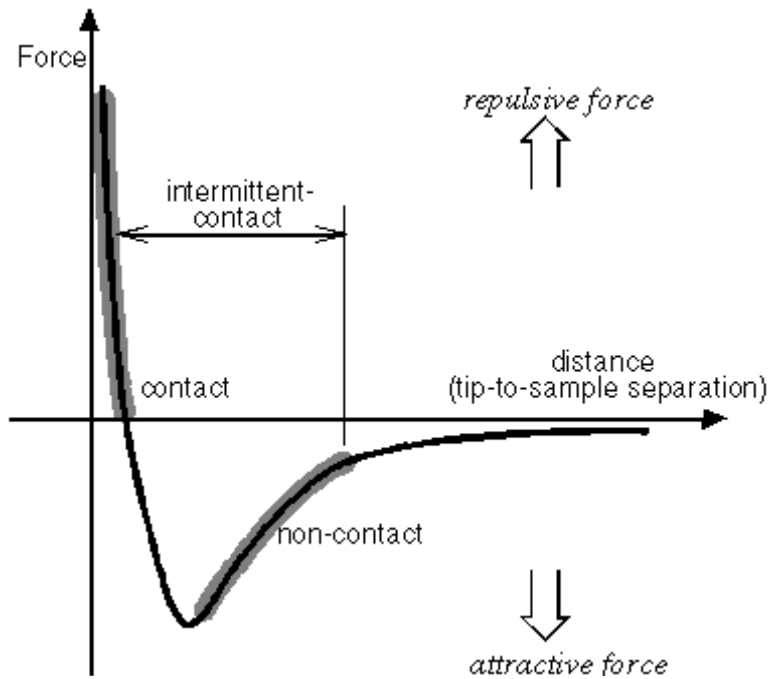


Fig. 6. Interatomic forces versus distance curve.

Two distance regimes are labeled on Figure 6

- The contact mode
- The non-contact mode/tapping mode.

In the contact mode, the cantilever is held less than a few angstroms from the sample surface, and the interatomic force between the cantilever and the sample is repulsive.

This type of imaging mode can achieve lattice resolution with adequate noise isolation.

This mode of operation can be destructive to the surface, especially with softer samples.

The other two modes are the tapping and the non-contact; in both modes, the interatomic force between the cantilever and the sample is attractive. Both of these modes of operation utilize an oscillating cantilever. The primary difference in these two modes is the amplitude of the oscillations, tapping uses amplitude of 20-100 nm while non-contact uses amplitudes of less than 10 nm.²⁷ For the purposes of this research, tapping mode was used to identify the topographical features of our samples.

Tapping Mode AFM

Tapping mode is a key advance in AFM. This potent technique allows high resolution topographic imaging of sample surfaces that are easily damaged, loosely held to the surface, or difficult to image by other AFM techniques. Tapping mode overcomes problems associated with friction, adhesion, electrostatic forces, and other difficulties that can plague conventional AFM scanning methods by alternately placing the tip contact with the surface to provide high resolution and then lifting the tip off the surface to avoid dragging the tip across the surface.²⁹ It also reduces tip wear which degrades image quality on rigid hard surfaces. This is especially important for the surfaces in this study.

Tapping mode imaging is implemented in ambient air by scanning a tip attached to the end of an oscillating cantilever across the sample surface. The cantilever is oscillated at or slightly below its resonance frequency with amplitude ranging typically from 20 nm to 100 nm. The tip may slightly “tap” on the sample surface during scanning, contacting the surface at the bottom of its swing.²⁷ During scanning, the vertically oscillating tip alternately contacts the surface and lifts off, generally at a frequency of 50,000 to 500,000 cycles per second. As the oscillating cantilever begins to intermittently contact the surface or feel an increased force from proximity to the surface, the cantilever oscillation is reduced due to energy loss caused by the tip feeling a force of contacting the surface. The reduction in oscillation amplitude is used to identify and measure surface features.

The feedback loop maintains constant oscillation amplitude by maintaining a constant RMS of the oscillation signal acquired by the split photodiode detector. Selection of the optimal oscillation frequency is software-assisted and the force on the

sample is automatically set and maintained although adjustments can be made by the operator. When the tip passes over a bump in the surface, the cantilever has less room to oscillate and the amplitude of oscillation decreases. Conversely, when the tip passes over a depression, the cantilever has more room to oscillate and the amplitude increases causing the feedback to move the tip closer to maintain the constant oscillation amplitude.²⁹ The vertical position of the scanner at each (x, y) data point in order to maintain a constant “setpoint” amplitude is stored by the NanoScope III controller electronics to form the topographic image of the sample surface. By maintaining constant oscillation amplitude, a constant tip-sample interaction is maintained during imaging.²⁷

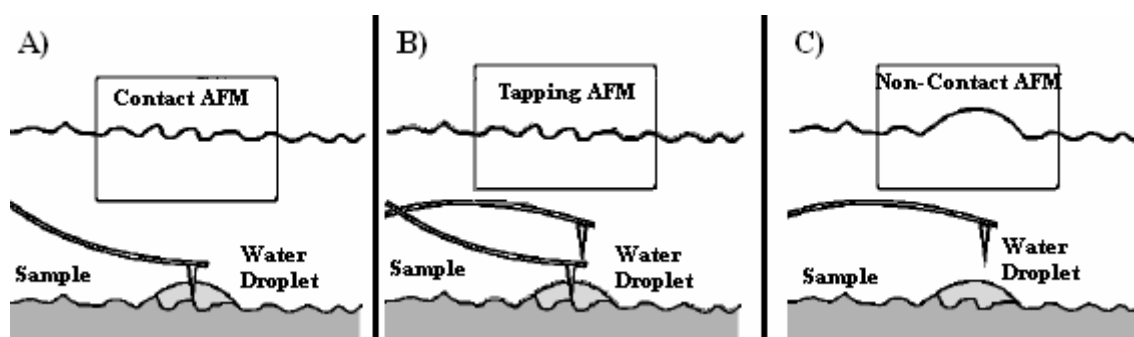


Fig. 7. AFM scanning modes. (A) Shows an AFM cantilever in constant contact with the surface and the image returned above. (B) AFM in tapping mode and hopeful representation of the surface above. (C) Failure of non-contact mode of operation for AFM notice the water droplet is reported as part of the surface.

Probe Tip Characterization

One of the most important factors influencing the resolution which may be achieved with an AFM is the sharpness of the scanning tip.³⁰ The geometry of the contact formed between the AFM tip and sample surface is not defined if the tip shape is not known. Furthermore the exact chemical composition of the tip is not easy to determine.³¹ The first tips used by the inventors of the AFM were made by gluing diamond onto pieces of aluminum foil. Commercially fabricated probes are now primarily used. The best tips may have a radius of curvature of only around 5nm.³⁰ A topographic AFM

image is actually a convolution of the tip and sample geometry.³¹ The term convolution is often used to group together any influence which the tip has on the image.

The main influences are

- Broadening
- Compression
- Interaction forces
- Aspect ratio

Tip broadening arises when the radius of curvature of the tip is comparable with, or greater than, the size of the feature trying to be imaged. Compression occurs when the tip is over the feature trying to be imaged. Interaction forces between the tip and sample are the reason for image contrast with the AFM. However, some changes which may be perceived as being topographical may be due to a change in force interaction.³⁰ Other forces are due to chemical interactions between the tip and surface, electrostatic interactions, or capillary forces when the tip encounters a water layer on the surface.

Separation of the tip and sample contributions by contact imaging sharp or at least known sample features allows, *in situ*, some determinations of the overall tip shape on a nanometer to micrometer scale. *Ex situ* tip imaging by transmission electron microscopy has also been performed. Some of these measurements have revealed that a majority of micro fabricated cantilevers possess double tips and other unsuitable tip structures. This shows that tip characterization is necessary for absolute measurements, but other means have been shown to be reliable for relative measurements.³¹ This work relies primarily on relative measurements although the use of calibration samples allow quantitative measurements with accuracies of 10-20%.

The tip that was used for this study was a Veeco ULNC-AUHW. It is a boron (p) doped Si with a cantilever thickness of 1.8 – 2.2 μm , because of the size of the cantilever, it has a smaller radius of curvature hence its ability to resolve smaller features. The tip is changed regularly as broadened tips have difficulty in resolving smaller features.

CHAPTER 3

EXPERIMENTAL PROCEDURE

In this chapter, the procedures used to prepare samples for the nanoparticle synthesis will be discussed. Some of the instruments used in the experiments have operation and procedure manuals located on the Physics Department webpage (<http://uweb.txstate.edu/%7eab35/manuals/manuals.htm>).

Sample Substrates

The Si (3 inch) wafers were obtained from a vendor. They were made of a silicon substrate (500 – 550 μm thick), with a 3000 Å silicon dioxide layer on top of the silicon. The silicon substrates were crystalline, with an orientation of (1 0 0). They were p-type boron doped silicon with resistivities of 10 – 20 ohm-cm.

Silicon Deposited by Ion Beam Deposition

To deposit an ultrathin Si layer on top of the oxidized Si substrates, they were mounted in the DIBS vacuum chamber for deposition. In order to clean the substrate of any contamination such as moisture or hydrocarbons, after pumping the chamber the substrate was heated at 300°C for 30 minutes in vacuum with pressure of $\sim 10^{-6}$ Torr. The sample was then allowed to cool down to room temperature. This was followed by O₂ atomic source cleaning (or pre-sputtering) for 20 minutes. This process removes any remaining contaminants from the substrate surface prior to deposition.

The pre-sputtering was done with an O₂ gas flow rate of approximately 5 sccm and an RF power of 200W. At this point, the substrate was ready for the Si deposition to begin.

In the preliminary studies, the thickness of the sputtered silicon was of much concern as there is no *in situ* film thickness measurement during the deposition. To address this, two separate samples were prepared for sputtering. The first few samples were to be used in the study of the sputtered thin silicon layer thickness by using x-ray diffraction (XRD). Tantalum was deposited first on the substrate before sputtering the thin silicon layer. This tantalum interlayer was to help use the XRD to measure the thickness of the deposited silicon, as the XRD could not differentiate the SiO₂ from the deposited Si. The tantalum was sputtered for 180 seconds and the silicon sputtered for 60 seconds. This was done under a very high vacuum (base pressure of 3.0×10^{-7} Torr) and a working pressure during deposition of 3.2×10^{-4} Torr. Argon gas was used to sputter these films with a gas flow rate of 8 sccm.

Additional samples prepared were to be annealed to form the nanoparticles. These samples had only silicon sputtered on the SiO₂ (no Ta deposited); the depositions were done for 30 seconds and 60 seconds respectively. The samples were left in the vacuum chamber until some few minutes before annealing. This was done in order to prevent the growth of any native oxide on its surface. The samples were cleaved into smaller sizes after being removed from the DIBS vacuum chamber for individual annealing.

The parameters for each of the sputter depositions (Ta/Si, Si for 60 seconds, Si for 30 seconds respectively) are presented in Tables 1 – 3. Photographs of the DIBS system are presented in Figure 8 showing both external and internal views.

Table 1. DIBS Specification for the Ta/Si Deposition

Base Pressure	3.0E-7 Torr
RF Power	150 Watts
Beam Current	61mA(Ta)/51mA (Si)
Accelerator Current/Voltage	8mA/0.259kV(Ta), 4mA/0.274kV (Si)
Ar gas flow rate	15.0sccm/10.0sccm
Working pressure	7.0E-4 Torr (Ta)/3.2E-4 Torr (Si)
Neutralizer filament current	5A
Pre-sputtering Time	5 minutes
Sputtering Time	3min (Ta)/ 1min (Si)

Table 2. DIBS Specifications for 60 second Si Deposition

Base Pressure	3.0E-7 Torr
RF Power	150 Watts
Beam Current/Voltage	53mA/0.76keV
Accelerator Current/Voltage	5mA/0.198kV
Ar gas flow rate	8sccm
Working pressure	3.2E-4 Torr
Neutralizer filament I	5A
Pre-sputtering time	5min
Sputtering Time	1min

Table 3. DIBS Specifications for 30 second Si Deposition

Base Pressure	3.2E-7 Torr
RF Power	150 Watts
Beam Current/Voltage	53mA/0.78keV
Accelerator Current/Voltage	5mA/0.175Kv
Ar gas flow rate	8sccm
Working pressure	3.2E-4 Torr
Neutralizer filament I	5A
Pre-sputtering time	5min
Sputtering Time	30 Seconds

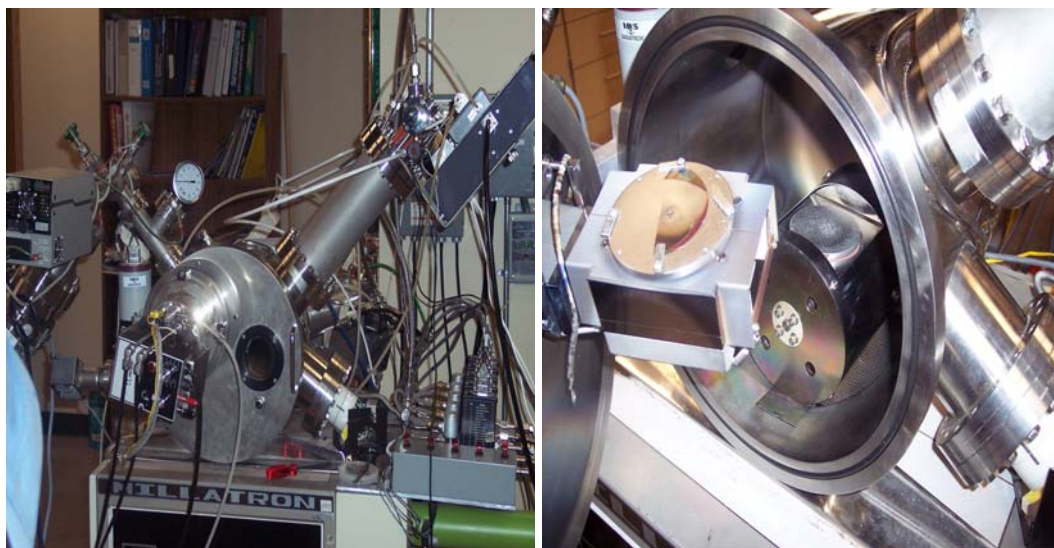


Fig. 8. DIBS ion source and vacuum chamber. (left) showing the ion source, the vacuum chamber and the residual gas analyzer. (right) inside the vacuum chamber, with the sputter targets and the sample holder.

X-ray Diffraction

As already mentioned, for the preliminary studies, the greatest concern was about the structure of these samples and the thicknesses of the sputtered tantalum and silicon layers. First of all it was necessary to make sure that the sputtered tantalum and silicon were actually present and to determine what thicknesses had been deposited. Two different characterization tests were made on the samples using the Bede Scientific X-ray Diffraction System. These included high angle x-ray powder diffraction (HAXRD), and x-ray reflectivity (XRR). Extensive discussion including the theory and operation of the x-ray diffractometer can be found in previous theses.

The sample was mounted with a double-sided tape on the sample stage and the appropriate instrument and sample alignments were done. The centered omega scan (angle of incident) was undertaken in the scan window, these alignments were repeated until the peak of the omega scan occurred at approximately zero. This was followed with

the 2 theta-omega scan where the detector was moved 2 degrees for every one degree that the sample was rotated in order to collect the diffracted x-ray signal for analysis.

With the HAXRD measurements, the system was set for the θ - 2θ measurement: the beam was then diffracted off the surface of the sample. The diffracted beam was picked up by the detector and the patterns analyzed by the software. The intensity in counts per second (cps) versus the angle 2 theta omega in degrees was measured. The resulting data graph was compared to the International Center for Crystal Diffraction Data (ICDD). This process was used in the determination of the sample lattice (including crystal planes identified by Miller indices). Three different samples were characterized. These included the 60-second before annealing, the 30-second annealed sample and the annealed 60-second sample respectively.

The XRR can give information on film thickness, roughness, and the formation of interfacial compounds. The XRR measurement was used to determine the thickness of each layer formed between the substrate and the surface layer. For this scan, the x-ray beam was incident at a critical angle; this caused a reflection and created interference patterns. This scan depends on the index of refraction of the material which is based on the electron density. From this pattern, properties of the sample such as the thickness and density can be determined by fitting the data to a computer model.

The XRR data were analyzed by using a computer simulation, REFS Mercury manufactured by Bede Scientific (Englewood, CO). The thickness of the film was found by changing the parameters until an appropriate fit was made. The sample characterized using this procedure was the tantalum-silicon sample. These data were later compared with the SIMS measurements.



Fig. 9. Bede Scientific XRD instrument with the hood and the sample stage. (left) the instrument with the x-ray isolation hood on. (right) close up of the optics stage, sample mounting stage and the detector stage.

Rapid Thermal Annealer

The rapid thermal annealer was used to anneal the samples for brief periods to high temperatures. This action causes the ultrathin Si films on top of the oxide layers to form nanoparticles.

Before samples were mounted in the RTA (Total Fab Solution Heatpulse 610), their surfaces were blown clean with nitrogen gas. This was done to remove any particles that have settled on the samples during the cleaving. The samples were annealed at different temperatures and different times. The temperatures for annealing were 900°C, 850°C, 800°C, 750°C, 700°C, 650°C and 600°C. Different samples from each anneal temperature were annealed for either 60 seconds or 30 seconds.

The samples were mounted in the chamber of the RTA one at a time, and argon gas was allowed to run through the chamber for minutes to purge it of air (oxygen and nitrogen). A particular recipe in the RTA computer was used to select the desired

temperature and time at which the samples should be annealed; the parameters of this recipe are shown in Table 4 below. After annealing, the samples were allowed to cool down in the chamber to approximately 80°C under Ar gas flow before they were removed.

Table 4. Parameters of the AGTEST recipe

	Type	Time/Rate	Temp.	Sensor	T _{sw}	Gain	DGain	Iwarm	Icold
1	Dly	60		Pyro					
2	Ramp	50	750*	Pyro					
3	SS	60*	750*	Pyro	90	-50	-5	2050	2050
4	Dly	900							

Note: * - Time and temperature would be changed according to the ones desired, it all depends on the annealing conditions.



Fig. 10. The Total Fab Solution RTA System. (left) with its computer software. (right) RTA chamber with the sample stage.

Atomic Force Microscopy

To determine the size and other characteristics of the synthesized nanoparticles, an atomic force microscope was used. All the samples were studied using the Veeco Dimension 3100 Nanoscope IV AFM. All the imaging was done in the tapping mode, with a Veeco ULNC-AUHW tip. The sizes of the scanned areas were typically $1\mu\text{m} \times 1\mu\text{m}$, $5\mu\text{m} \times 5\mu\text{m}$, or $10\mu\text{m} \times 10\mu\text{m}$.

To make sure that the studies done on the AFM were accurate, a controlled experiment was performed on a sample. The sample was scanned before and after annealing without any deposited film. Images were taken and compared to the other samples that had silicon deposited on them.

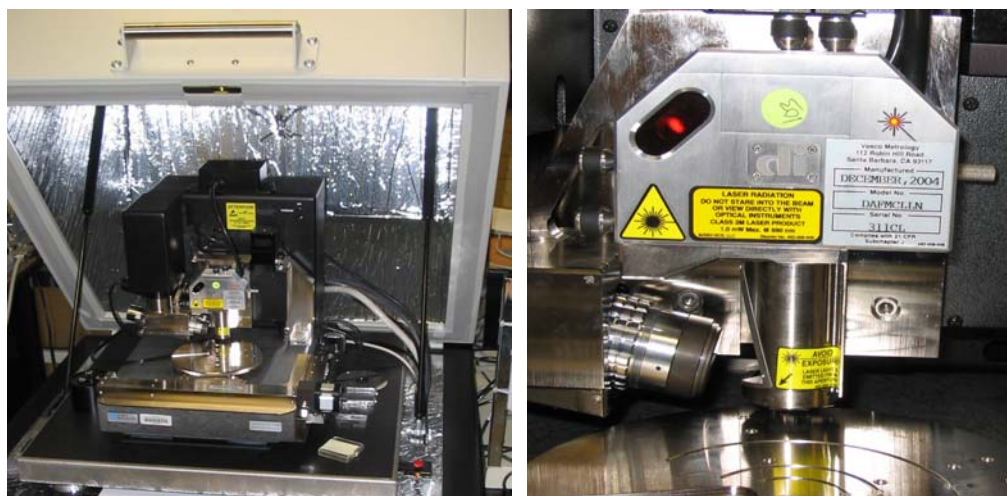


Fig. 11. Veeco AFM and Scanner Head. (left) noise isolation table and hood with scanner head and sample chuck, (right) close up of scanner head and optical focusing system visible to on left side of the scanner head.

CHAPTER 4

DATA AND ANALYSIS

In this chapter, the data collected during nanoparticle synthesis and characterization will be presented. First, the methods used to determine the thicknesses of the very thin Si layers at the top of the SOI substrates is given. After this, the AFM characterization of the resulting nanoparticles is presented.

Layer Composition

In order to determine the composition of our sample layers, an HAXRD measurement was performed on some of the initial Si/Ta samples that were prepared. This was done to help in verifying two things. Firstly, to determine whether the deposition process was successful and to measure the Si layer thickness and determine a sputter deposition rate for these sputter parameters. Finally, it could determine whether after the annealing process, all the expected layers still existed. This scan was taken with the incident beam at an angle to the film equal to that between the film and the detector.

Table 5. Color code of samples characterized by the x-ray diffractometer, with time and temperature of anneal

Color Code	Sample ID	Temperature of Anneal	Time of Anneal
Blue	Si060831_01aa001.X01	--	--
Red	Si060831a30s_01aa001.X01	900°C	30 seconds
Green	Si060831a60s_01aa001.X01	900°C	60 seconds

Figure 12 shows HAXRD scans of the samples in Table 5; a graph of 2 theta in degrees was plotted against the intensity in cps for each of these samples. From this figure, sample blue was shown to have a very low intensity throughout the entire scan. However after annealing of this same sample, there were increases at certain angles. For example, on the 2 theta axis, at an angle of ~ 44.0 degrees, the intensity of sample green was approximately 2350 cps. The structure of the sample at this angle was identified as Ta_3Si . For this same angle, the intensity of sample red is approximately 1200 cps. This leads to the conclusion that the sputtered layers of Ta and Si were still present before and after annealing. This figure also shows that the annealing has produced various alloys of Ta and Si. The unannealed sample showed negligible amounts of Ta_3Si while the alloy formation was driven by the anneal and the Ta_3Si intensity was seen to increase with annealing time. Nanoparticles formed from these samples will be alloys of these two elements.

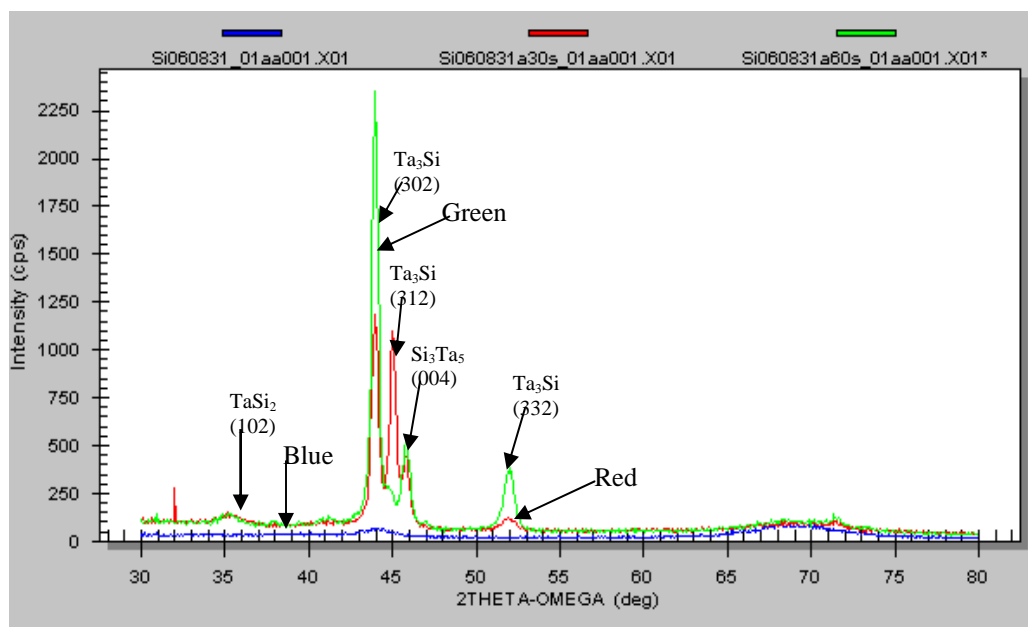


Fig. 12. HAXRD scans for Ta and Si layers. Sample blue shows an unannealed sample while red and green indicates annealing at 30 seconds and 60 seconds respectively. The scans indicate the composition of each of these samples.

Depth Profiling

The size of nanoparticles formed depended on certain conditions, one of these conditions being the thickness of the layer of the deposited silicon. Due to this reason, it was imperative that the thickness of this should be measured.

The x-ray reflectivity (XRR) measurement was used to determine the thickness of the tantalum and silicon layers. On this sample, tantalum was deposited for 3 minutes followed by a 60-second silicon deposition using conditions listed in Chapter 3. The XRR data was entered into the REFS Mercury computer simulation and the thickness of the films were found by changing the parameters until an appropriate fit was achieved.

Figure 13 and Table 6 shows the data fit of the XRR scan.

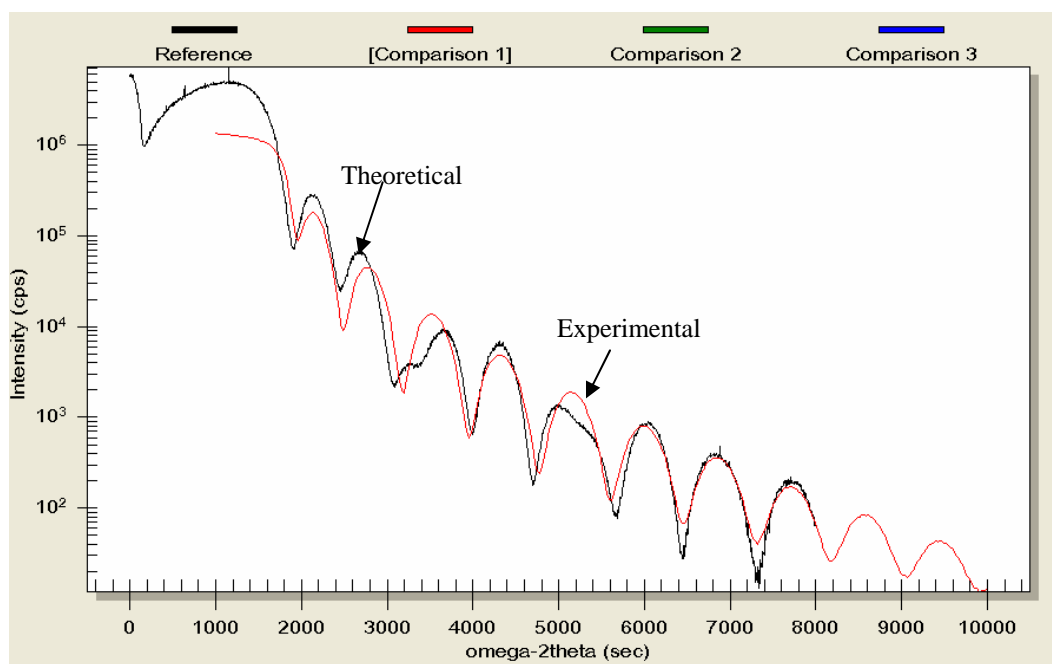


Fig. 13. REFS computer modeling for Ta and Si.

Table 6 REFS computer data fit for Ta and Si

Model														
	THICKNESS (Å)	fix	low	high	MATERIAL	X	fix	low	high	Y	fix	low	high	DENS
5	1.00	<input checked="" type="checkbox"/>	1	5	SiO2	▼ 0.000	<input checked="" type="checkbox"/>	0	0	0.000	<input checked="" type="checkbox"/>	0	0	100.00
4	100.00	<input checked="" type="checkbox"/>	50	150	Si	▼ 0.000	<input checked="" type="checkbox"/>	0	0	0.000	<input checked="" type="checkbox"/>	0	0	100.00
3	1.00	<input checked="" type="checkbox"/>	1	5	Ta2O5	▼ 0.000	<input checked="" type="checkbox"/>	0	0	0.000	<input checked="" type="checkbox"/>	0	0	100.00
2	179.31	<input type="checkbox"/>	150	400	Ta	▼ 0.000	<input checked="" type="checkbox"/>	0	0	0.000	<input checked="" type="checkbox"/>	0	0	98.94
1	3057.51	<input type="checkbox"/>	2500	4000	SiO2	▼ 0.000	<input checked="" type="checkbox"/>	0	0	0.000	<input checked="" type="checkbox"/>	0	0	99.91
SUB.	∞	<input checked="" type="checkbox"/>	∞	∞	Si	0.000	<input checked="" type="checkbox"/>	0	0	0.000	<input checked="" type="checkbox"/>	0	0	100.00

According to the data obtained from Table 6, the thickness of the deposited Ta layer was approximately 179.3 Å and the deposited layer of Si was approximately 100.0 Å. A very thin layer of Ta₂O₅ was also observed, with a thickness of 1 Å; the reason for this tantalum oxide layer between the Si and Ta is not known. Since this deposition took place in a vacuum, a tantalum oxide layer was not expected. There was a thin layer of native oxide with thickness of 1 Å. This layer of native oxide was due to the fact that the sample was left in the atmosphere for sometime before this characterization took place. It should be emphasized that this process is not the best approach in characterizing the thickness of thin layers. Due to this, further characterizations of the thicknesses were done with the SIMS depth profiling analysis.

As already mentioned, an effective way to characterize the sputtered layer thicknesses of the samples was required. This was due to the fact that the thickness of the sputtered silicon layer had a direct effect on the sizes of nanoparticles produced. Since SIMS depth profiling is a very accurate method to characterize thicknesses of thin layers, there was no need to deposit tantalum between the SiO₂ and the thin Si layer.

Two separate samples were characterized using the SIMS in the Process and Characterization Lab (PCL) of International Sematech. Both samples had only a thin silicon layer deposited on the SiO₂, with the deposition times of 30 and 60 seconds

respectively. Figures 14 and 15 shows graphs of counts per second versus depth in nm for these two samples.

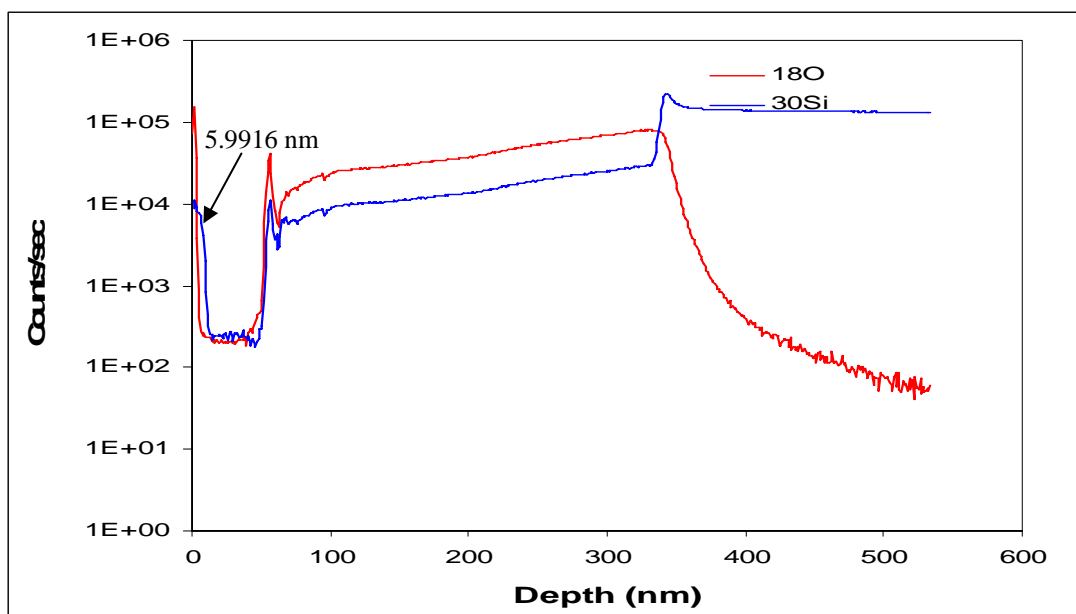


Fig. 14. A depth profile of a 30-second deposition of silicon on an SiO₂ substrate.

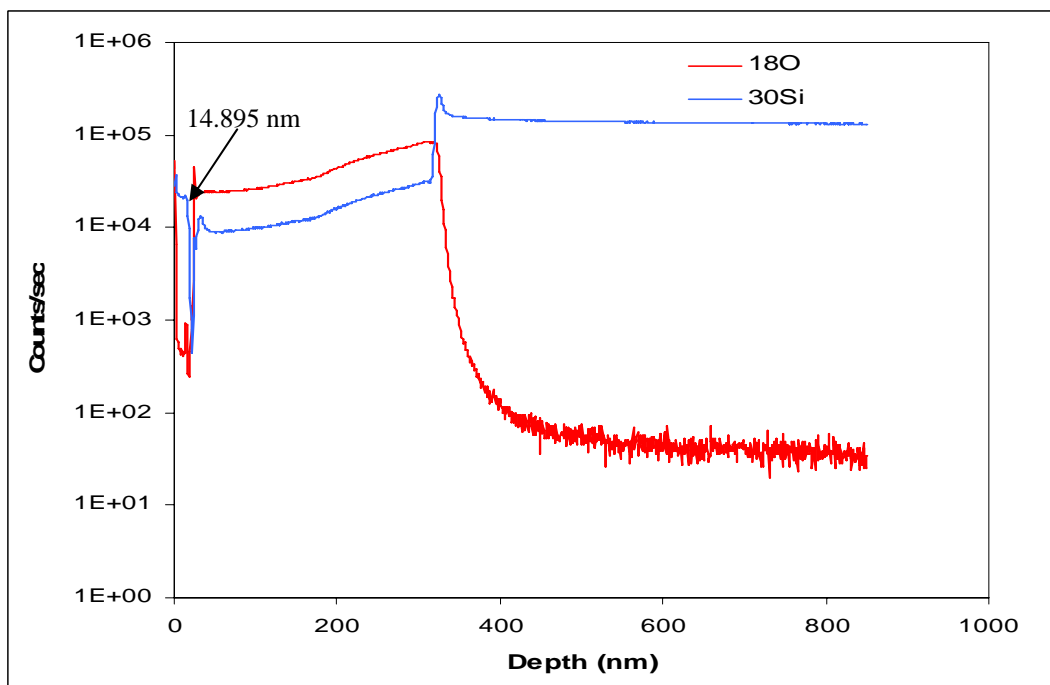


Fig. 15. A depth profile of a 60-second deposition of silicon on an SiO₂ substrate.

Figure 14 indicates a deposited silicon layer thickness of ~6.0 nm; this deposition was done in 30 seconds. Since the sample was left in the atmosphere before the depth profiling, a considerable amount of oxide was formed on the silicon layer. This is also indicated in the graph with the red color. The gap present in the data may be due to problems with the cleaning process before deposition (involving carbon). On Figure 15, the sputtered silicon layer thickness was ~14.9 nm, this sputtering took place for 60 seconds. Again a considerable amount of native oxide grew on top of the sputtered silicon layer prior to measurement.

Since the time for deposition varied for these two samples, it was expected that they would have different thicknesses. This also confirms that the thickness of the sputtered layer depends on the duration of deposition. Finally, comparing the XRR method and the SIMS approach, it can be concluded that, the 60-second deposition for the XRR and SIMS approach gave different Si thicknesses of 10 and 15 nm respectively. This can be attributed to the fact that the XRR method is not an accurate process of determining the thicknesses of thin layers.

Nanoparticle Size Distribution

The basic phenomenon that drives nanoparticles formation is associated with minimization of the free energy of the Si/SiO₂ system³⁷. A simple model is shown on Figure 16 below. Starting from a volume V of a silicon film, associated with thickness d_{si} on top of an oxide layer and a surface area of S, a nanoparticle with a semispherical-like shape of radius r is formed. The energy variation ΔE between the initial and the final states is given by the equation

$$\Delta E = (\sigma_{co}\pi r^2 + \sigma_c\pi r^2) - (\sigma_{co} + \sigma_c) S, \quad (1)$$

where σ_{co} and σ_c are the silicon-silicon oxide interface energy and the free silicon energy, respectively.

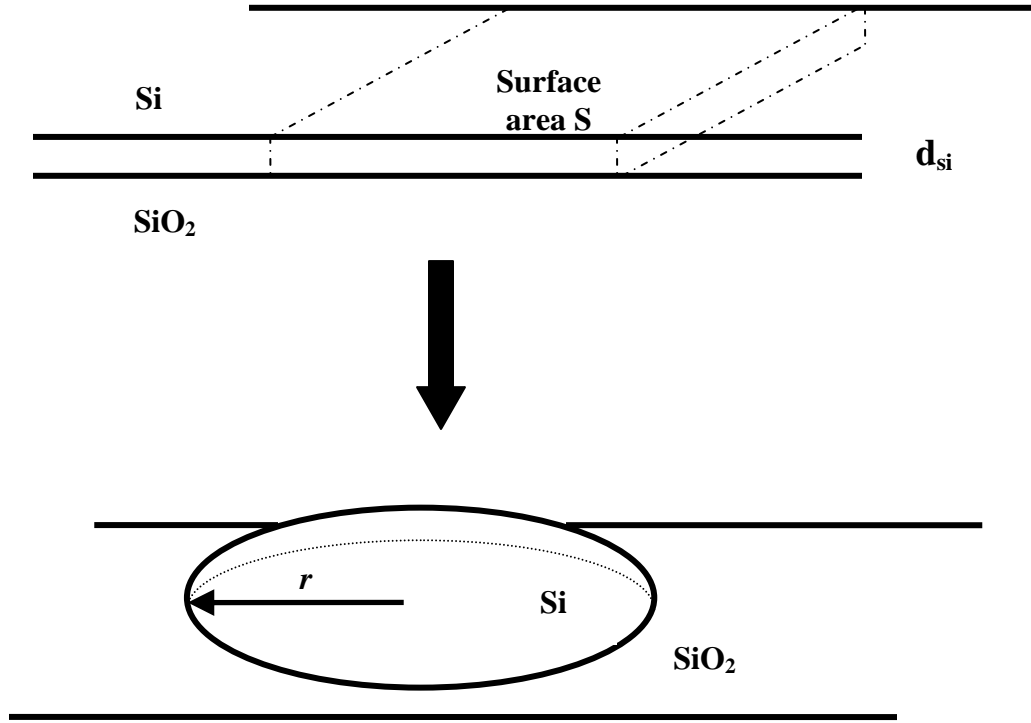


Fig. 16. Schematic of nanoparticle formation.

Taking into account that $Sd_{si} = \frac{2}{3} \pi r^3$, and making $\Delta E < 0$ in the case of island formation, a simple relationship that gives a minimum radius r_m associated with the formation of nanoparticles was found:

$$r_m = \frac{3d_{si}}{2} * \frac{\alpha + 2}{\alpha + 1}, \quad (2)$$

where $\alpha = \sigma_{co} / \sigma_c$.

The interface energy σ_{co} is of the order of 0.3 J/m, and σ_c is of the order of 0.75 J/m.

These values lead to r_m of the order of 2.5 d_{si} . For $d_{si} = 14.9$ nm and 6.0 nm, r_m was

computed to be of order of 37.2 nm and 14.9 nm respectively. These r_m values are in agreement with the results of Legrand et al.²⁰

AFM Images

Unannealed and Annealed SiO₂ Control Samples

Two separate images of an unannealed SiO₂ and an annealed SiO₂ sample with annealing temperature of 850°C were taken using the AFM. This was a control experiment to confirm that the images seen after annealing a sputtered Si sample were not due to any artifacts of the AFM and especially to verify that no nanoparticles are formed merely by annealing an oxide film in Ar. Figures 17a and b shows the images of the SiO₂ and annealed SiO₂ respectively.

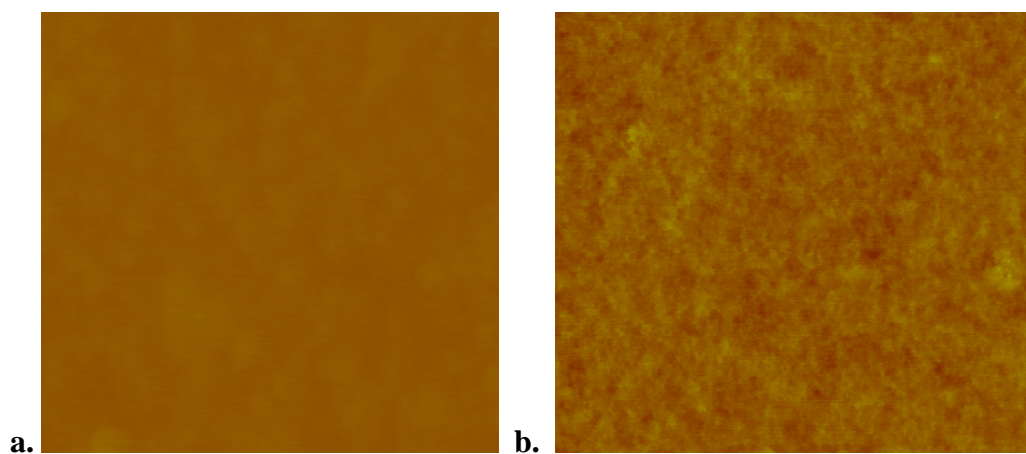


Fig. 17. AFM images for annealed and unannealed SiO₂ samples. (a) SiO₂ sample with oxide thickness of 3000Å, (b) Annealed SiO₂ sample. Both images are 1 x 1 μm².

The AFM analysis of the unannealed and annealed SiO₂ samples revealed that their surfaces were very flat and no nanoparticle formation was observed in the absence of a Si layer on top of the oxide. The RMS roughness for the unannealed and annealed SiO₂ were 0.19 nm and 0.25 nm respectively.

AFM Analysis of the 6 nm Si layer after Anneal

By using the AFM, it was possible to analyze the nanoparticle size distribution for various anneal temperatures using this Si layer thickness (6 nm). Figures 18 - 24 show the AFM images of seven samples annealed at different temperatures. The three images that were taken at each temperature had 1 x 1, 5 x 5 and 10 x 10 μm scan sizes respectively. The temperature of annealing of each of these samples was varied and the effect in particle size is very obvious. A peak-to-peak average measurement was taken on the resulting nanoparticles and a normal distribution was found using statistical packages for social sciences software (SPSS). Figure 25(a)-25(g) show the island size distribution graph for temperatures of 600, 650, 700, 750, 800, 850 and 900°C, respectively.

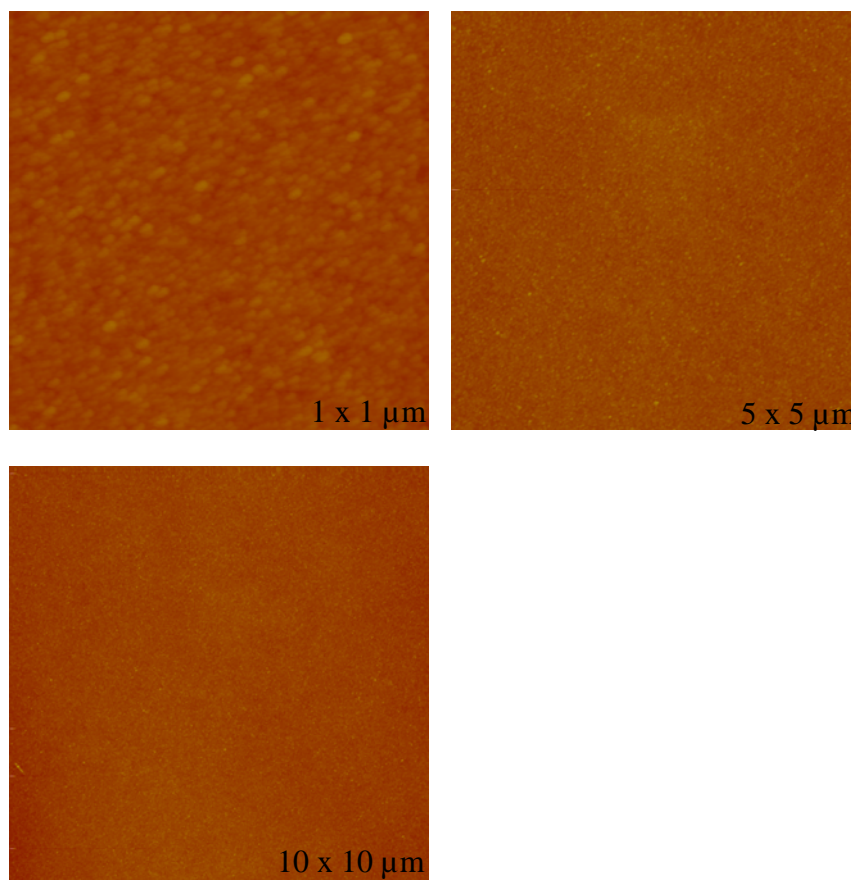


Fig. 18. AFM images for the 6 nm Si on oxide sample annealed at 600°C.

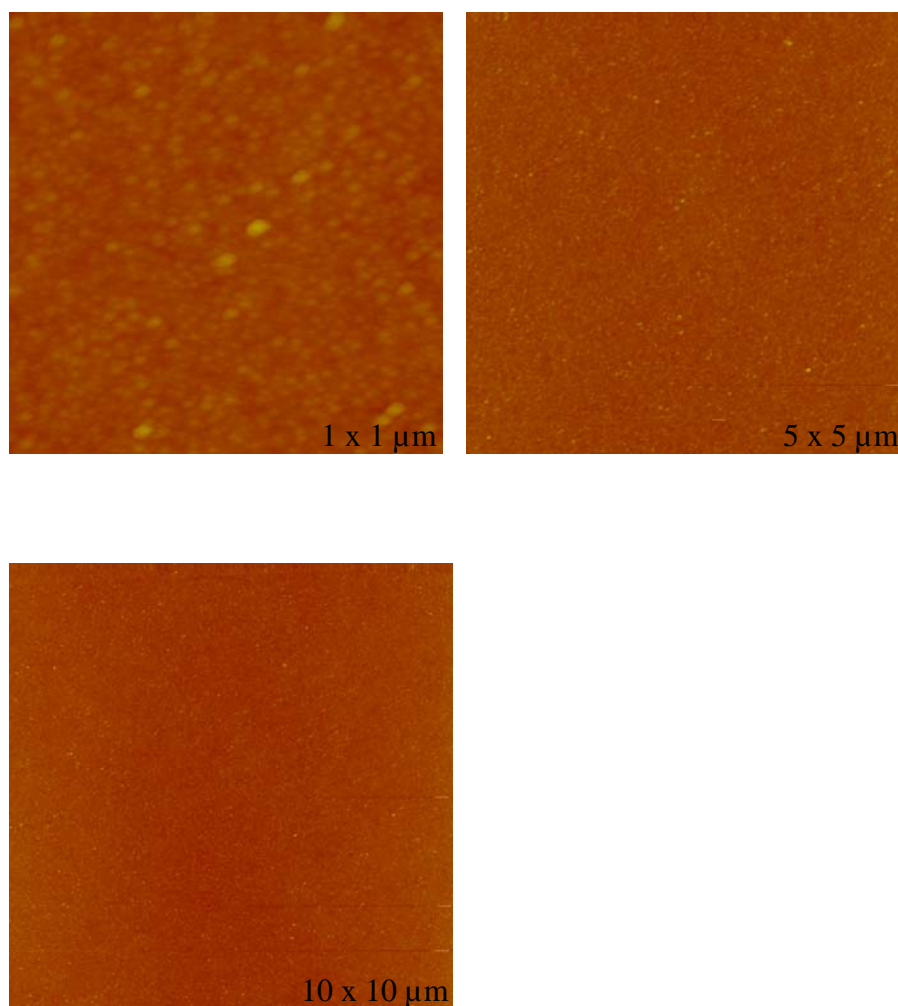


Fig. 19. AFM images for the 6 nm Si on oxide sample annealed at 650°C.

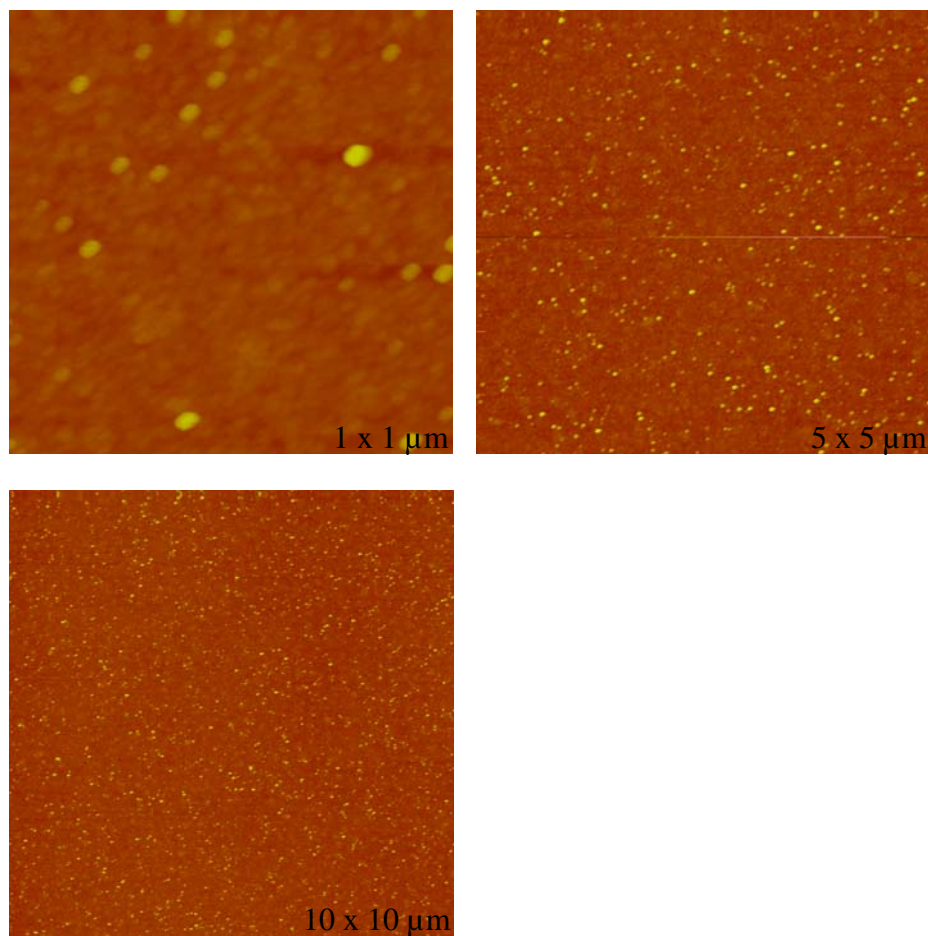


Fig. 20. AFM images for the 6 nm Si on oxide sample annealed at 700°C.

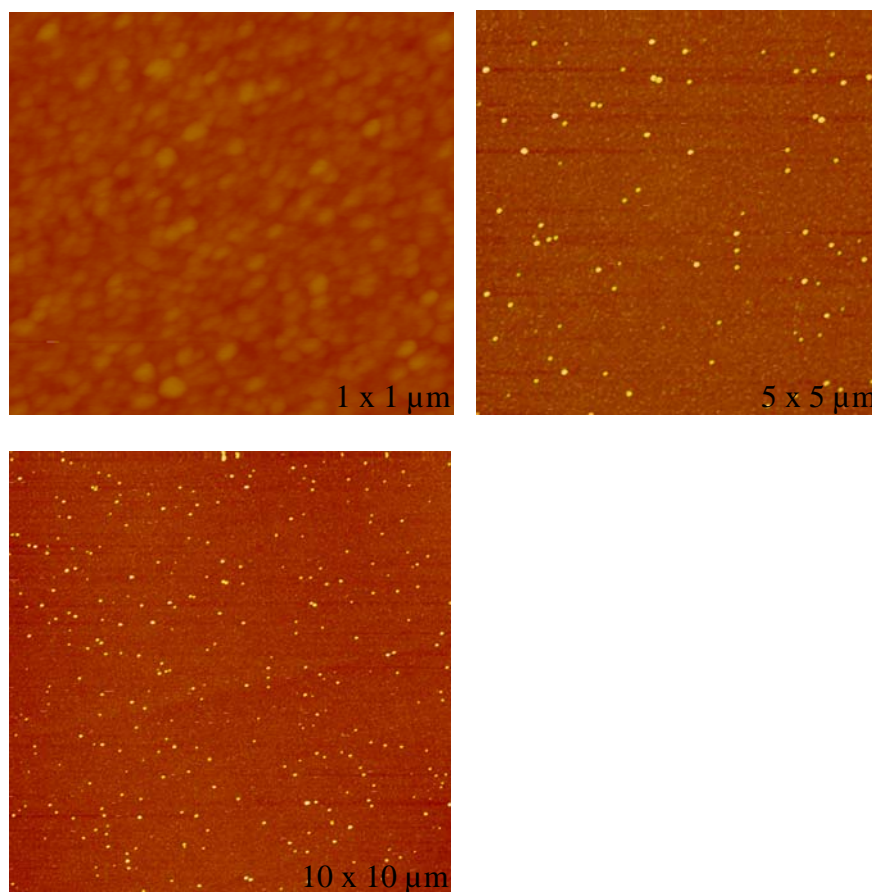


Fig. 21. AFM images for the 6 nm Si on oxide sample annealed at 750°C.

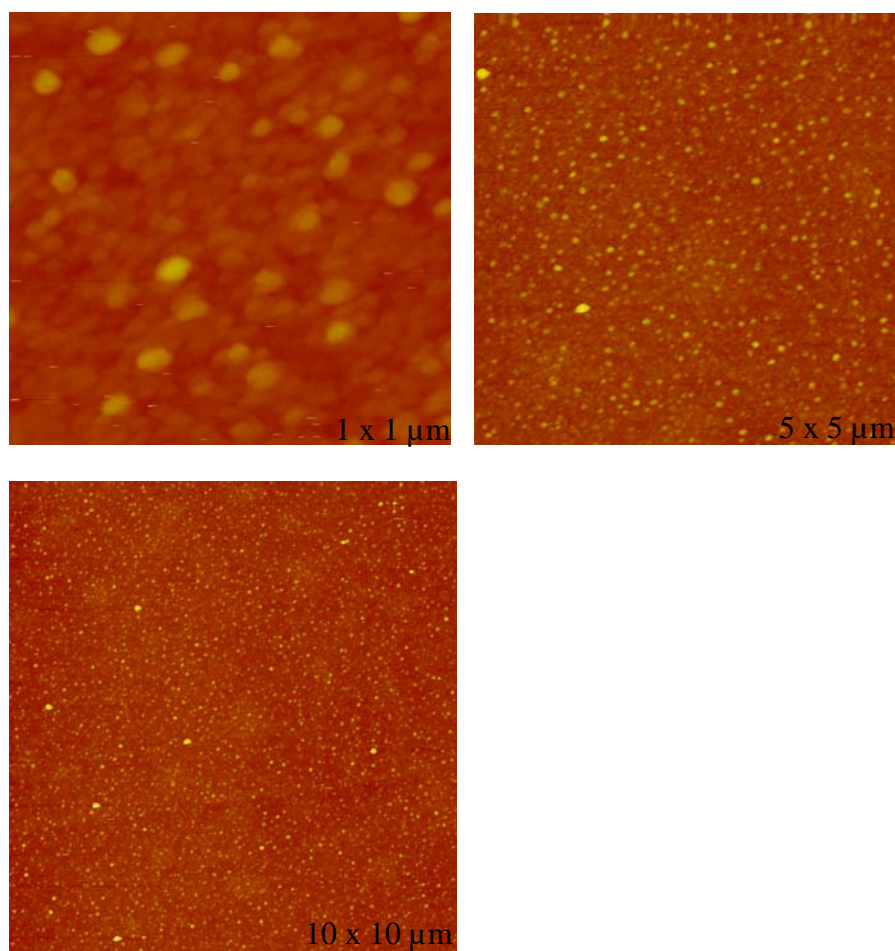


Fig. 22. AFM images for the 6 nm Si on oxide sample annealed at 800°C.

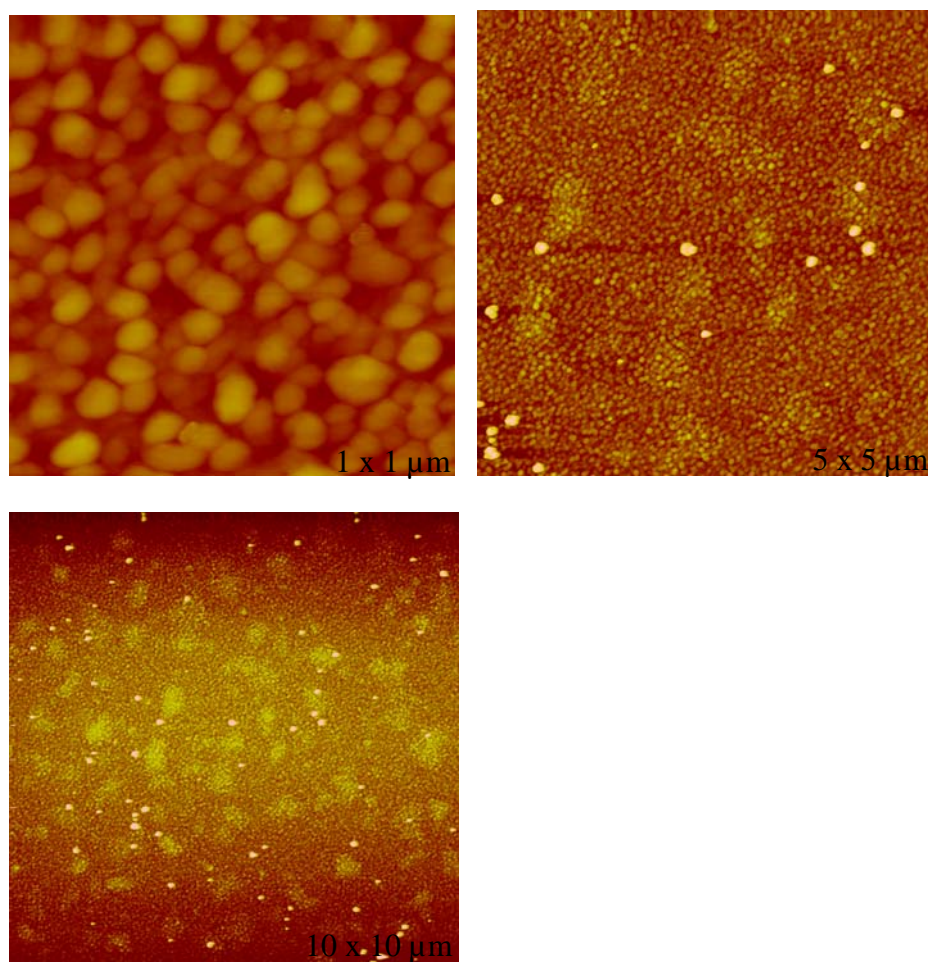


Fig. 23. AFM images for the 6 nm Si on oxide sample annealed at 850°C.

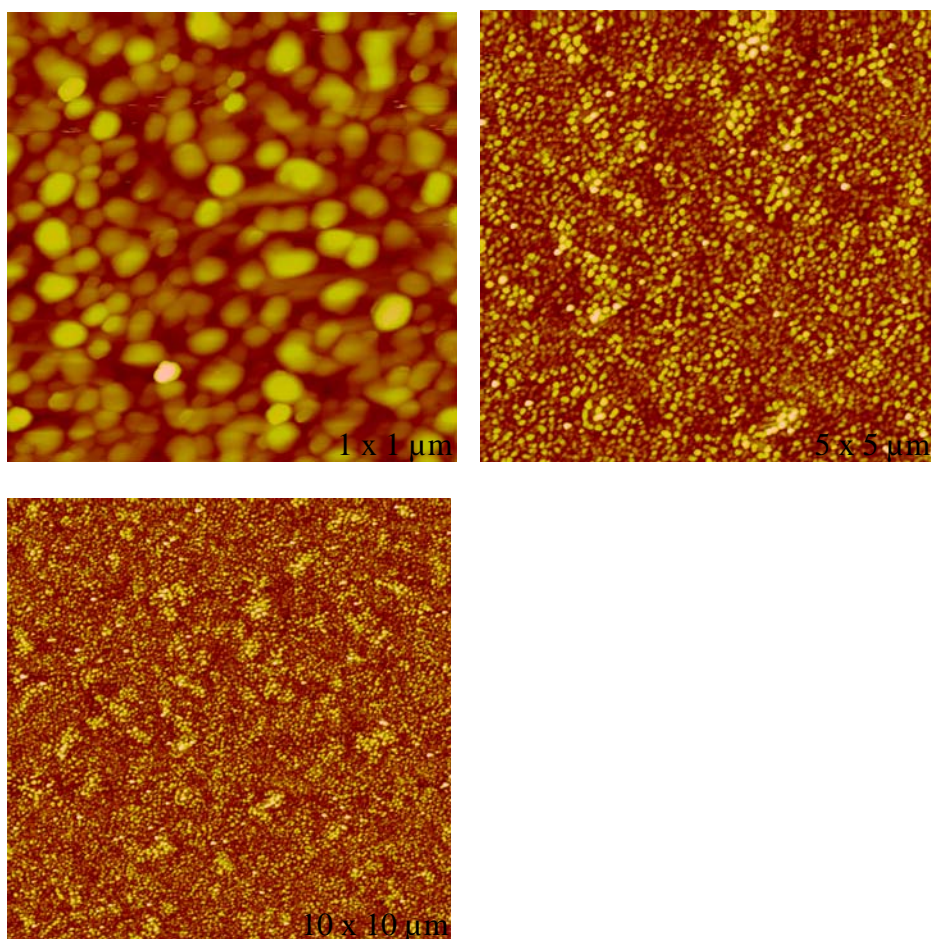


Fig. 24. AFM images for the 6 nm Si on oxide sample annealed at 900°C.

From Figures 25(a)-25(g), the size distribution of the various samples are presented. Typically, a measurement from the peak of one particle to the peak of the nearest particle was undertaken, this was done for 80 nanoparticles and their average radius was taken. By looking at the size distributions, it was found that the anneal temperature has an effect on the nanoparticle size. Higher anneal temperatures caused an increase in the radius of the nanoparticles, and at very high temperatures i.e. 850 to 900°C, the particles seems to agglomerate into bigger particles. The average particle radius of a sample annealed at 600°C was ~16.5 nm and that of 900°C was ~44.7 nm.

Figure 26 shows a graph of how the particle size changes with increase in annealed temperature.

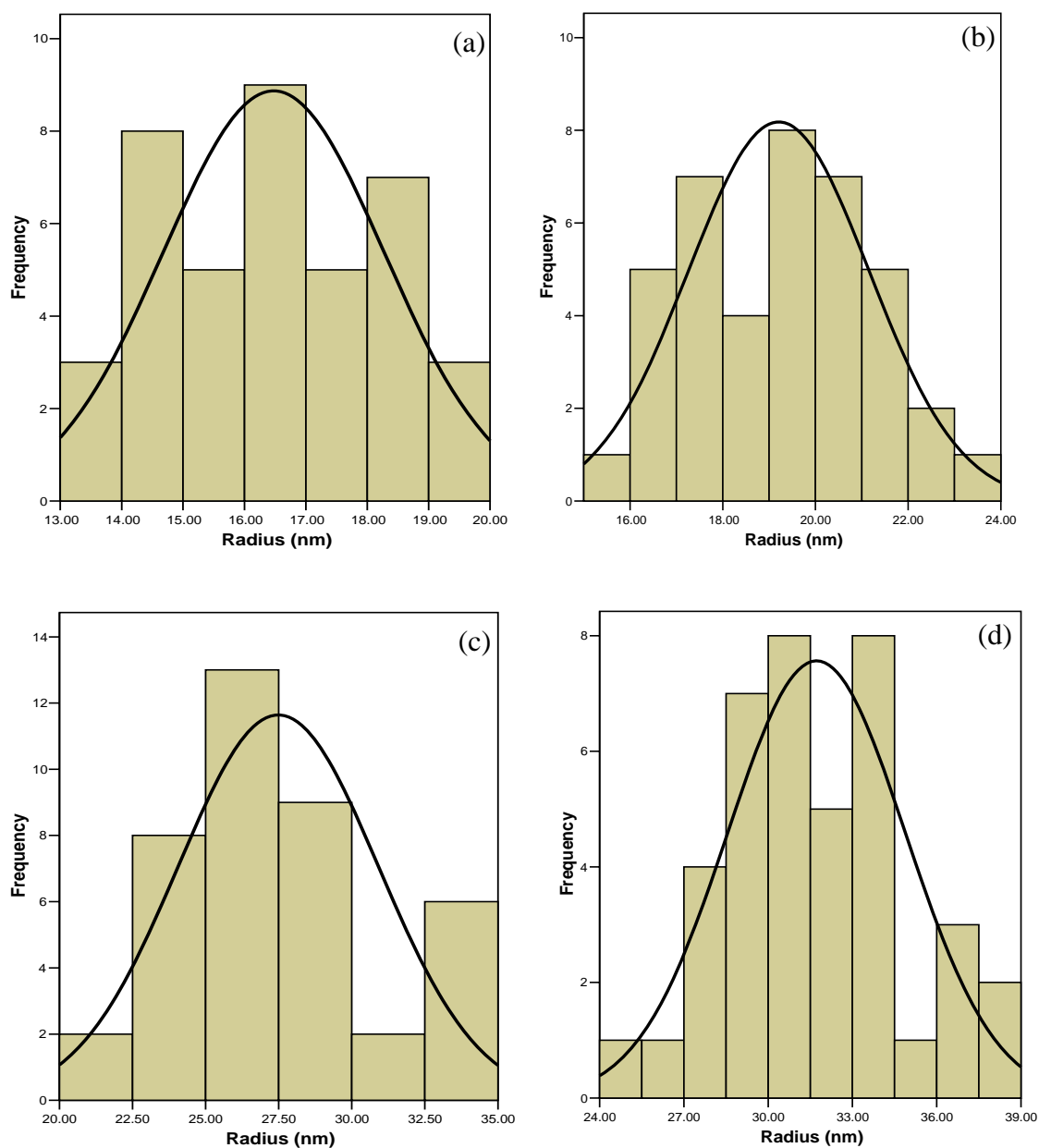


Fig. 25. Size distribution of the Si nanoparticles annealed at (a) 600°C, (b) 650°C, (c) 700°C and (d) 750°C. Lower temperatures produce smaller nanoparticles and higher temperatures resulted in the formation of larger nanoparticles.

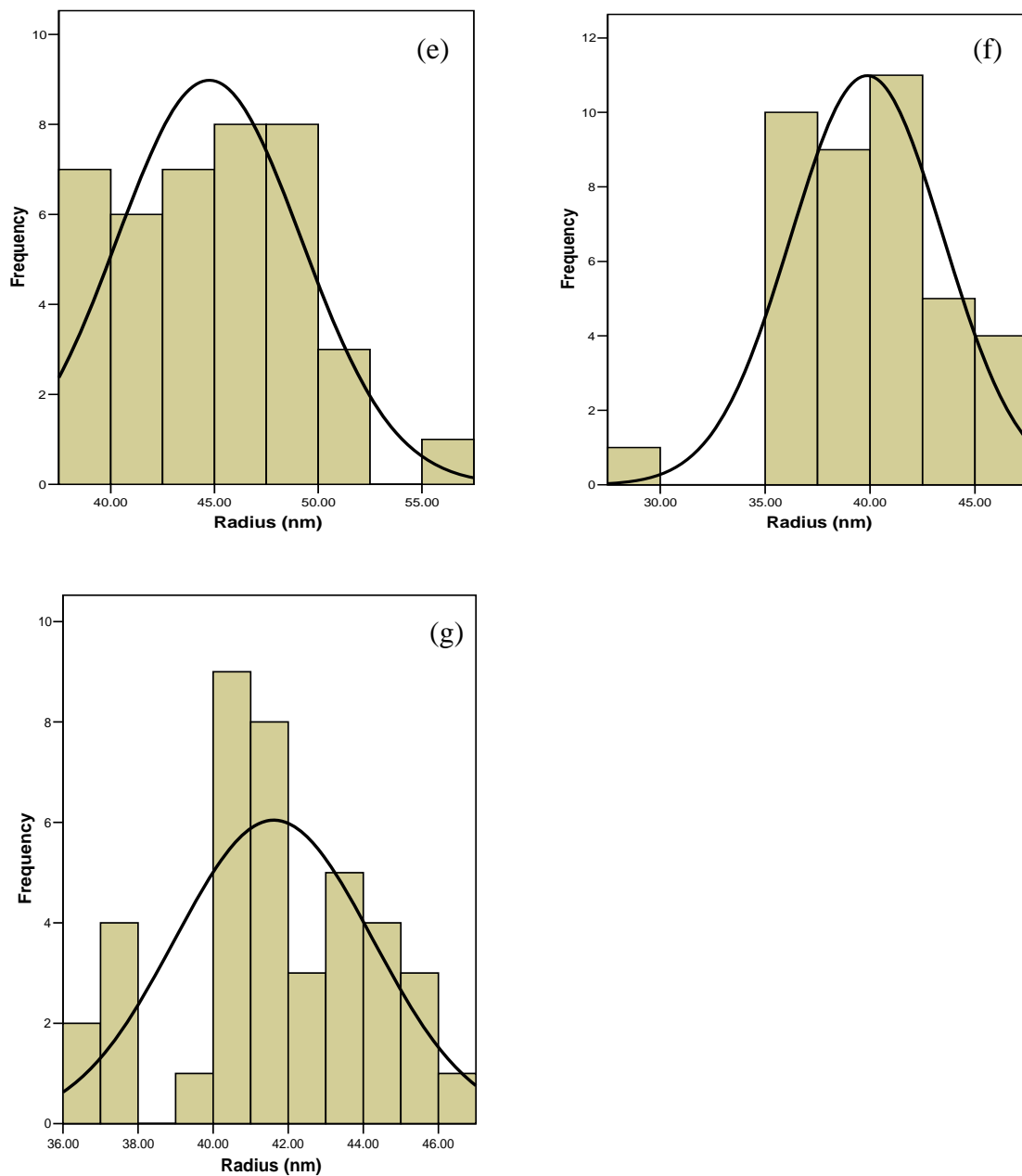


Fig. 25. Size distribution of the Si nanoparticles annealed at (e) 800°C, (f) 850°C and (g) 900°C. Lower temperatures produce smaller nanoparticles and higher temperatures resulted in the formation of larger nanoparticles.

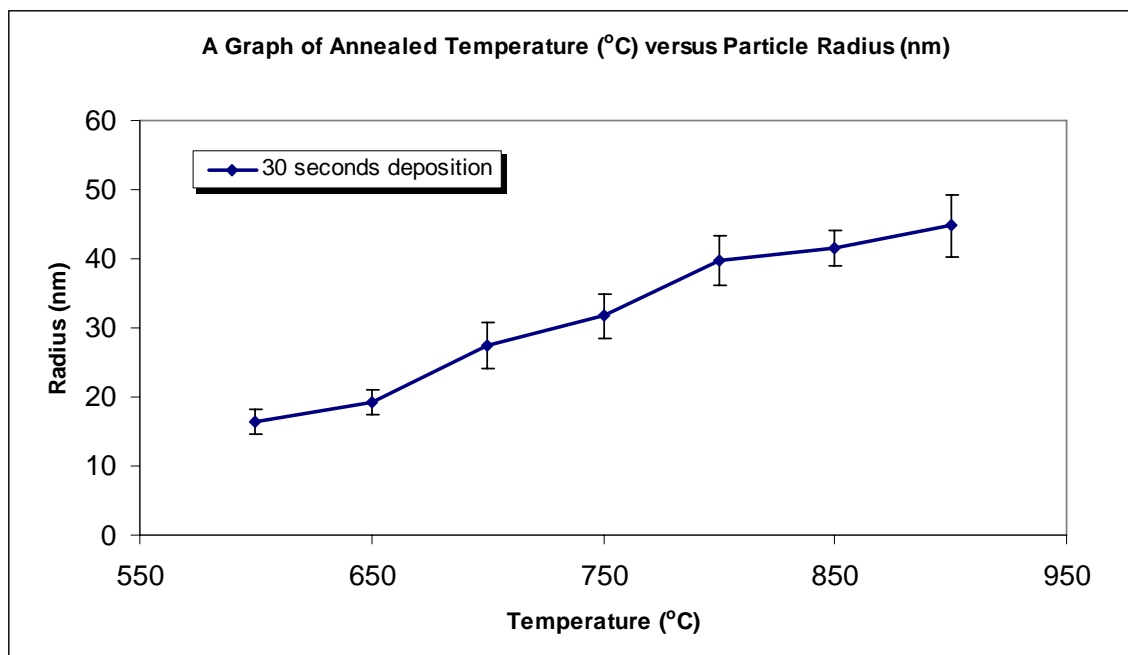


Fig. 26. A graph of temperature of anneal versus nanoparticle radius of silicon layer thickness of 6.0 nm.

AFM Analysis of the 15 nm Si layer after Anneal

The final set of samples which had a silicon layer of 15.0 nm were also characterized using the AFM. These samples were annealed at 600, 650, 700, 800, 850 and 900°C for 60 seconds. The scanned image size for these samples were 1 x 1, 5 x 5 and 10 x 10 μm , except the 850 and 900°C which had scans of 1 x 1 and 5 x 5 μm only. The scanned images are presented on Figures 27 – 32. Random measurements from the peak of one particle to that of the nearest particle were taken on 80 of the nanoparticles from each sample. Each of these values was divided by two to get the approximate radius of the particles. The SPSS software was used again to find normal distribution curves for the samples.

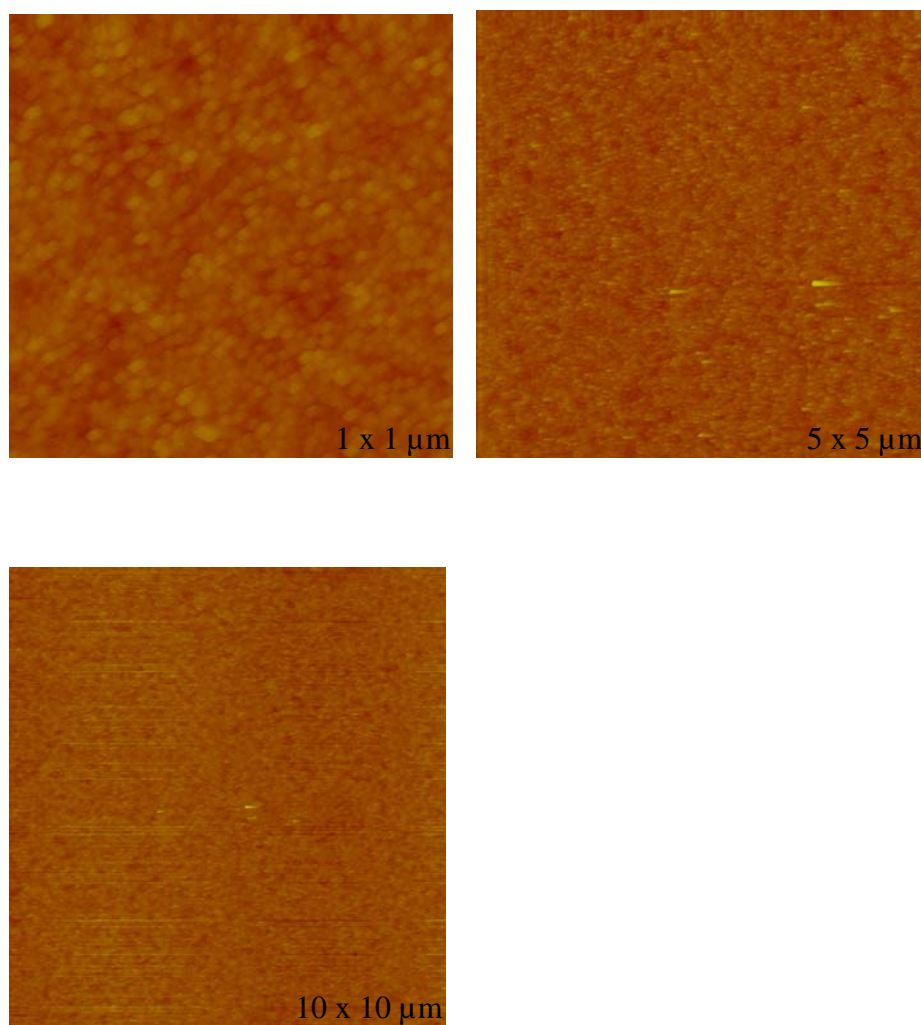


Fig. 27. AFM images for the 15 nm Si on oxide sample annealed at 600°C.

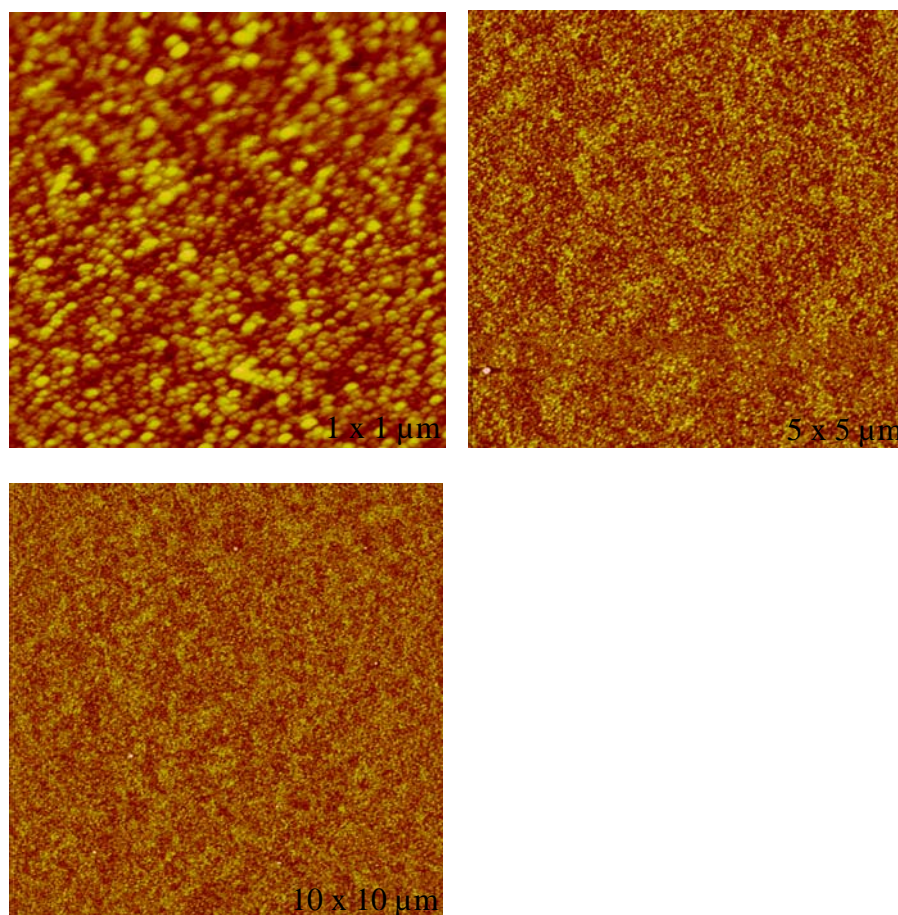


Fig. 28. AFM images for the 15 nm Si on oxide sample annealed at 650°C.

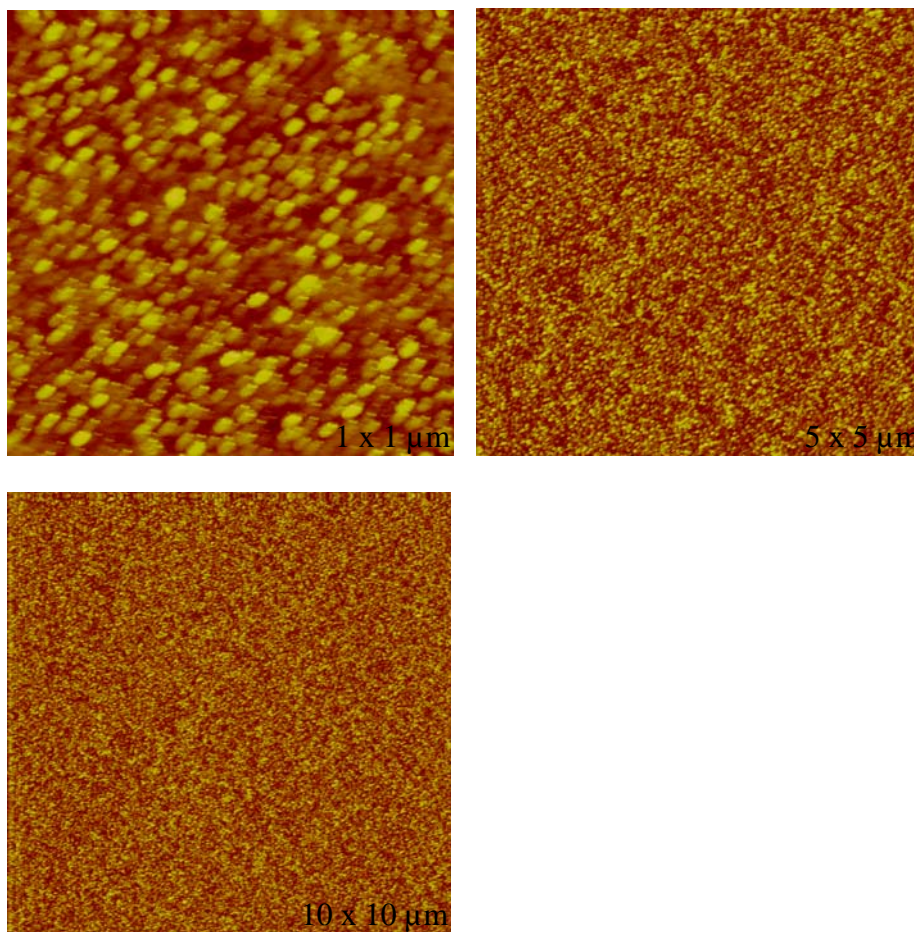


Fig. 29. AFM images for the 15 nm Si on oxide sample annealed at 700°C.

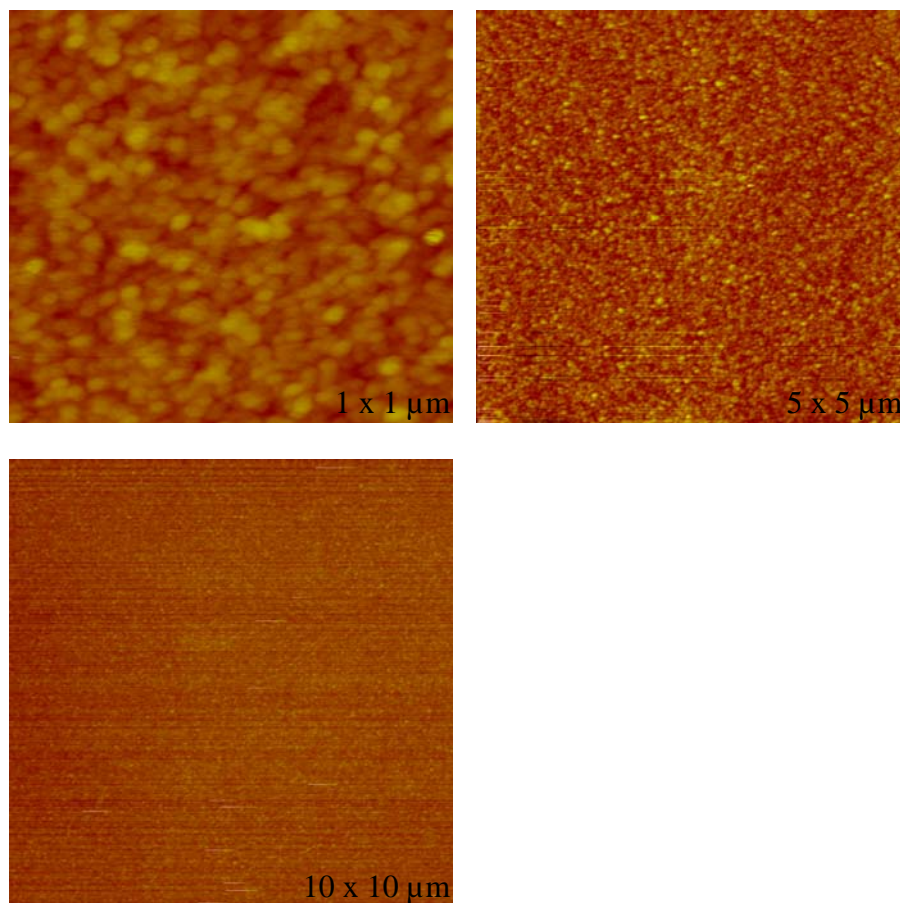


Fig. 30. AFM images for the 15 nm Si on oxide sample annealed at 800°C.

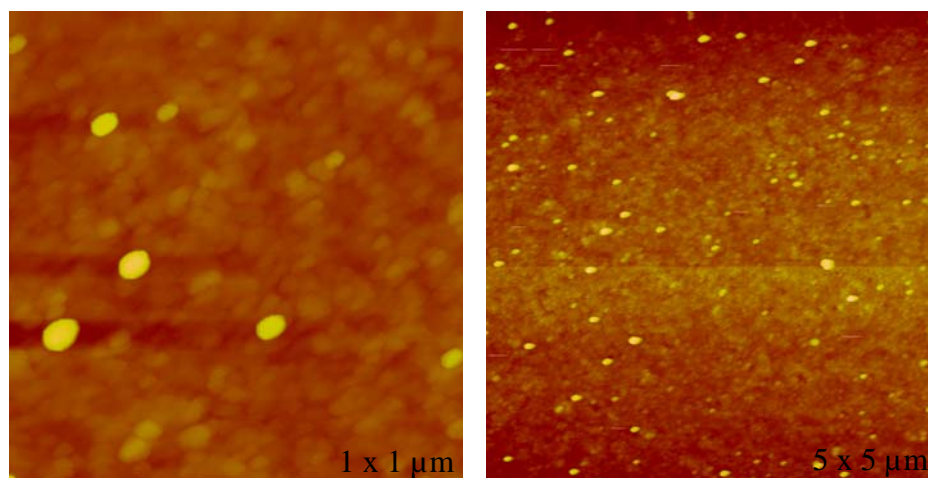


Fig. 31. AFM images for the 15 nm Si on oxide sample annealed at 850°C.

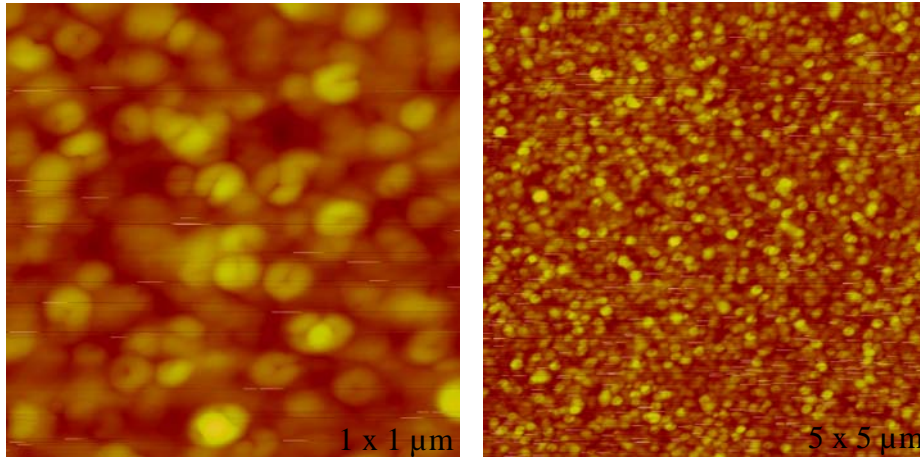


Fig. 32. AFM images for the 15 nm Si on oxide sample annealed at 900°C.

Figures 33(a)-33(f) show the normal distribution curves of frequency versus the radius (in nm) of the nanoparticles. This distribution indicates that the higher the temperature of annealing, the larger the nanoparticles size. The mean particle radius of 600°C was approximately 17.8 nm but as the temperature rises up to 900°C, the mean radius also increased to 56.3 nm. This is in agreement with our earlier, thinner samples. Figure 34 indicates how the change in anneal temperature affects the radius of the nanoparticles for this sample.

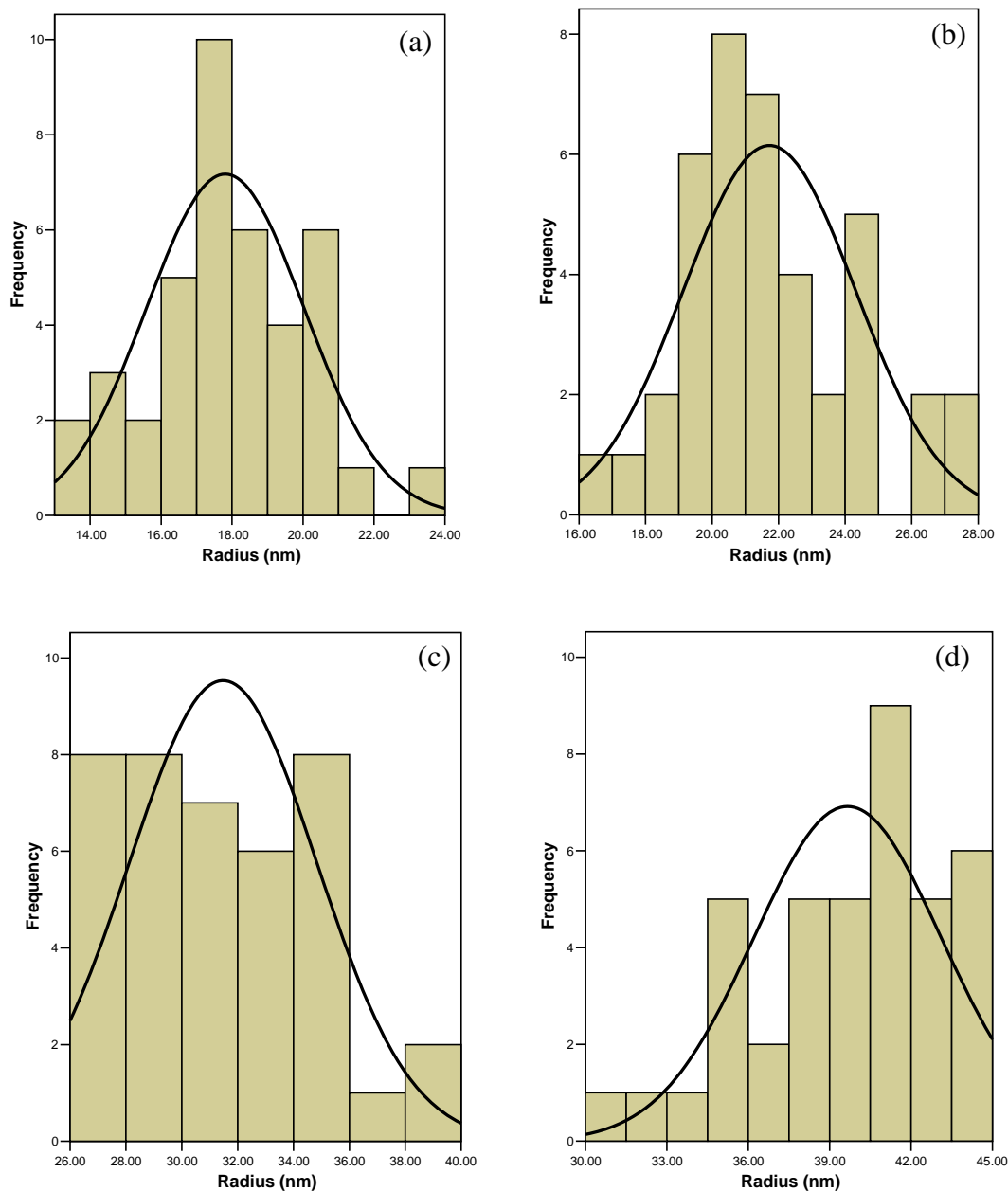


Fig. 33. Size distribution of the Si nanoparticles annealed at (a) 600°C, (b) 650°C, (c) 700°C and (d) 800°C. Lower temperatures produce smaller nanoparticles and higher temperatures resulted in the formation of larger nanoparticles.

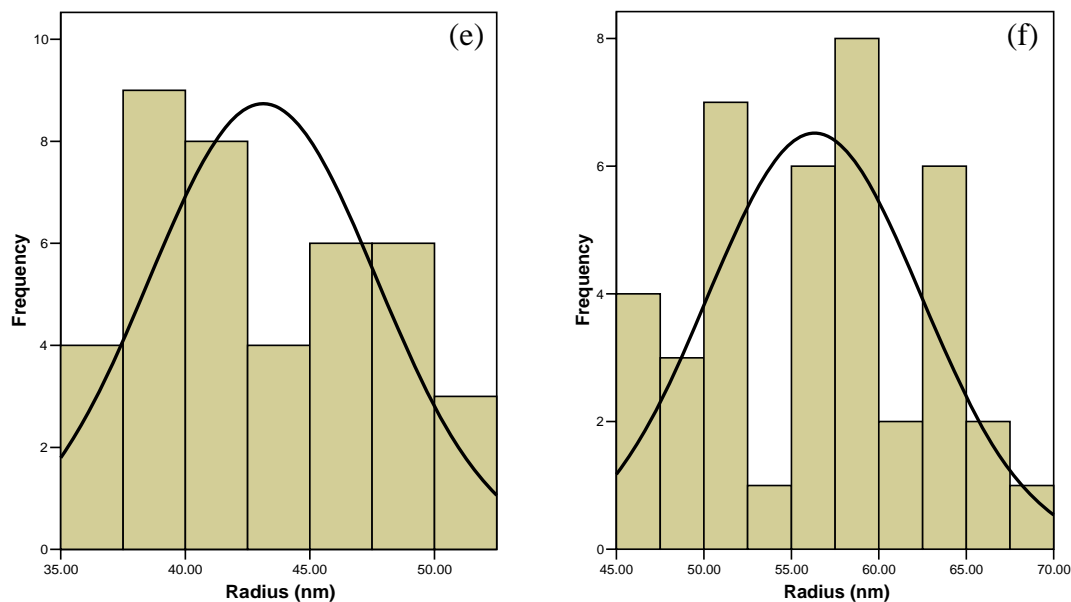


Fig. 33. Size distribution of the Si nanoparticles annealed at (e) 850°C and (f) 900°C. Lower temperatures produce smaller nanoparticles and higher temperatures resulted in the formation of larger nanoparticles.

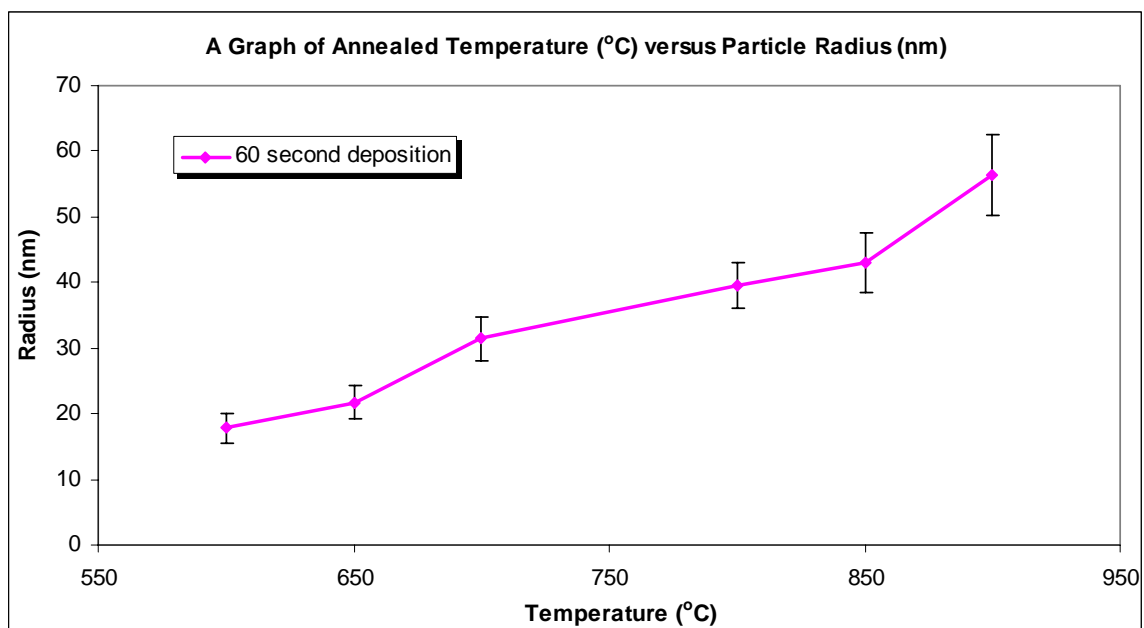


Fig. 34. A graph of temperature of anneal versus nanoparticle radius of silicon layer thickness of 15.0 nm.

Comparison of silicon layer thicknesses and anneal temperatures

Finally the effect of the silicon layer thickness on the size of the nanoparticles formed was studied. A graph of the particle radii versus temperature of anneal was plotted for both samples for comparison for the two results. In Figure 35, at 600°C the mean particle size for the 60-second anneal was larger than that of the 30-second anneal. This is realized throughout the plot, except at the 800°C where the two seem to be close. No explanation was found for this abnormality.

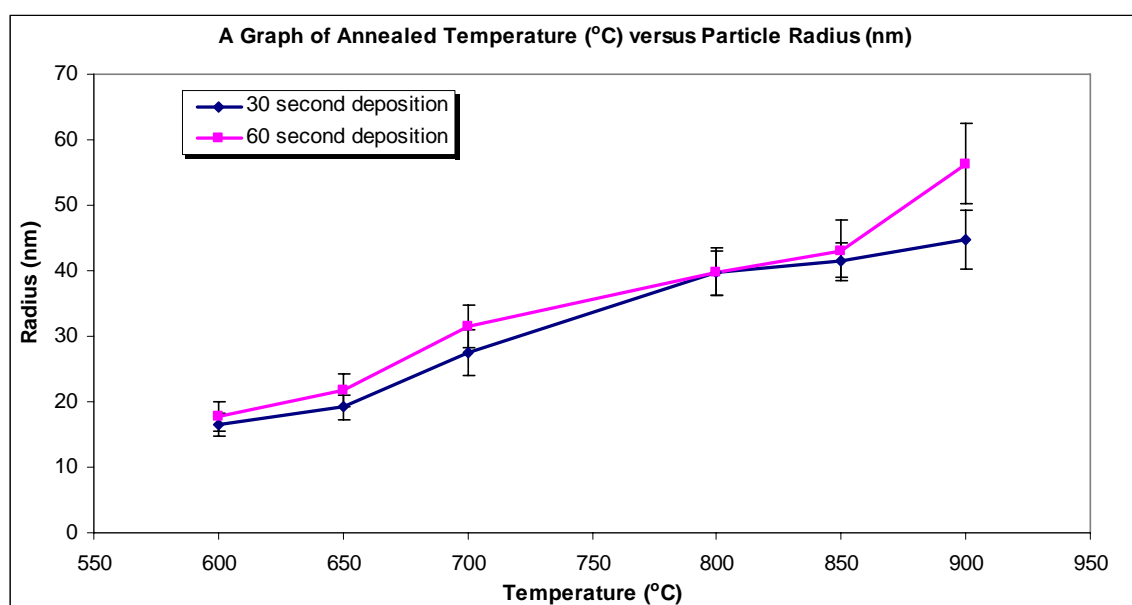


Fig. 35. A graph of temperature of anneal versus nanoparticle radius for both samples.

CHAPTER 5

CONCLUSIONS

In this chapter, the major results of the study are summarized. These primary results include the formation of nanoparticles in ambient pressure, size dependence on the anneal temperature and size dependence on the layer thickness. Suggestions for future studies have also been made.

This project has succeeded in the formation of silicon-based nanoparticles using the thermal annealing process at atmospheric pressure in an inert gas (Ar). It was found that this process was an acceptable method when compared to other thermal annealing processes in more constrained environments (low vacuum up to UHV). This method gave nanoparticle sizes and size distributions, as demonstrated by the AFM peak-to-peak measurements, comparable to other methods discussed. An important benefit of this method is that in an atmospheric pressure process, no UHV equipment is needed to synthesize the nanoparticles. It is also less expensive and faster to synthesize nanoparticles with this process. From a technological point of view, this study opens up a way to easily form silicon-based nanoparticles on an insulating substrate.

Secondly, these measurements successfully determined how the size of the nanoparticles formed directly depends on the temperature of annealing. It was found that the higher the temperature of anneal the larger the nanoparticle size. This was observed in

both of the SOI samples for annealing temperatures falling in the range between 600°C and 900°C in 50°C increments. With an annealing temperature of 600°C, the mean radius for the samples with an initial silicon layer thickness of 6 and 15 nm were 16.5 nm and 17.8 nm respectively. As the anneal temperature increases to 700°C, the mean radius for the samples also increase to 27.5 nm and 31.5 nm respectively. At 900°C, there is further increase in the mean radius to 44.7 nm and 56.3 nm respectively.

Finally, it was observed that the size of nanoparticles formed at each anneal temperature also depended on the thickness of the deposited silicon layer. The measurements show that the greater the thickness of the deposited silicon, the larger the size of the nanoparticles formed under similar conditions for all the samples being studied. The mean radius of the nanoparticles for the samples of 6 nm layer silicon thickness ranges from 16.5 to 44.8 nm and that for the samples with silicon layer thickness of 15 nm ranges between 17.8 and 56.33 nm. This was in agreement with other published data on the formation of silicon nanoparticles by thermal annealing.

A major question not answered in this project was the exact nature of the resulting nanoparticles. After annealing, are they Si nanoparticles, amorphous or crystalline or something else? When removed from the Ar atmosphere, are they completely oxidized or does a Si core remain? Future work on this technique should include the use of other methods to characterize the synthesized nanoparticles. These methods should include but not limited to the use of a scanning electron microscope (SEM) and transmission electron microscope (TEM). This will help in analyzing the particles from different perspectives and determine exactly what is being synthesized during the atmospheric anneal. Also, a better cleaning process prior to deposition of the silicon should also be of much concern

in any future studies. A clean surface before deposition is critical to the nanoparticles formed.

Additional work is needed to document how these particles could be put into device structures such as capacitors and transistors, and the performance of electrical characterization would be an ideal way to confirm the results.

APPENDIX A

RTA Operation Procedure

1. Start water chiller and wait for 5 minutes, turn on the second chiller.
2. Turn on the compressed air.
3. Turn on the power supply after which the computer can be powered on.
4. Use tweezers to pick up the sample and clean sample with dry N₂ gas before mounting in the RTA furnace.
5. Open the chamber slowly and place sample carefully on the stage. Close the chamber carefully to avoid any damage to the thermocouple.
6. Turn on the argon gas and let it run for 5 minutes to flush the chamber.
7. Adjust argon flow rate to 10-12 standard cubic feet per hour (scfh) on the scale and 5-6 standard cubic feet per minute (scfm) on the power supply.

Running Program

1. Open the computer program and press R on the keyboard. (R-read recipe)
2. Scroll through the various programs and select AGTEST recipe.
3. Adjust the parameters of the process to fit final temperature and temperature ramp requirements.
4. Press E on the keyboard to execute the recipe.
5. Press F1 on keyboard to run recipe.

APPENDIX B

AFM Operation Procedure

Tapping Mode

- 1 For this mode, use a Veeco ULNC-AUHW tip.
- 2 In the control panel choose "Tapping" for AFM Mode.

Mounting the probe into the cantilever holder

1. Use sharp tweezers to pick up the probe (make sure to hold the probe from the 2 long edges – do not touch the tip with the tweezers).
2. Make sure the probe is secured when loaded into the cantilever holder.

Loading the cantilever holder into the SPM

1. Make sure the SPM is not locked in its place (the knob located at the right should be tight).
2. Slide the SPM upward and out.
3. Carefully load the cantilever holder to the bottom of the SPM.

Aligning the laser to the tip

- 1 While looking at the trace of the laser beam, turn the upper knob at the top of the SPM clockwise until the intensity of the trace becomes very dim. Adjust the lower knob at the top of the SPM to find the shadow of the tip on the center of the beam's trace.

Adjusting the photodetector

- 1 Use the two knobs located at the left of the SPM to adjust the photodetector.
- 2 Adjust the knobs until the dot on the SPM display is centered.
- 3 In the meantime, look at the laser signal on the right monitor and try to center the red dot at the center of the cross.
- 4 Try to get ~0V vertical deflection.
- 5 Sum should be ~2.
- 6 Slide back the SPM. Carefully make sure the SPM is all the way in. Lock it by unscrewing the right knob.

Aligning the microscope to the tip

- 1 Select Stage/Locate Tip (or click the Locate Tip icon).
- 2 Center the cantilever under the cross hairs using the two knobs at the left of the optical objective of the microscope.
- 3 Focus the tip - Using the trackball, while holding down the bottom left button.

Load the substrate using tweezers and turn on the vacuum switch.

Focusing Surface

- 1 On the computer, go to Stage/Focus Surface.
- 2 Use the trackball and upper left button to move the wafer under the SPM.
- 3 Follow the instructions on the screen.
- 4 Focus on the sample by rolling the trackball up or down while pressing the bottom left button.
- 5 This adjustment raises or lowers the vertical engage stage on which the SPM and optics are mounted.
- 6 Be careful when doing this so that the tip does not hit the sample surface.
- 7 Move the desired measurement point under the cross hairs with the trackball without holding down any of the buttons.

Cantilever tuning

- 1 Go to View/Cantilever Tune (or click on the Cantilever Tune icon).
- 2 For Auto Tune Controls, make sure the Start Frequency is at 20 kHz and the End Frequency is at 70 kHz.
- 3 Target Amplitude for smooth surfaces should be 2-3 volts.
- 4 Target Amplitude for rough surfaces should be 0.5-1 volts.
- 5 Click on Auto Tune (a "Tuning" sign should appear then disappear once Auto Tune is done).
- 6 A single peak will appear with a resonance frequency between 220-320 kHz (If this does not occur, change the tip).
- 7 When done, quit the Cantilever Tune menu.

Setting initial scan parameters

- 1 In the Scan Controls panel, set the initial Scan Size to 1um, X and Y Offsets to 0, and Scan Angle to 0.
- 2 In the Feedback Controls panel, set Integral Gain to 0.4, Proportional Gain to 0.6, and Scan Rate to 1 Hz.
- 3 In the Channel 1 mode, set the Data Type to Height, Line Direction to Trace, Real Time Plane Fit to Line, Offline Plane Fit to Full, High Pass Filter Off, Low Pass Filter Off.

Engaging tip

- 1 Go to Motor/Engage (or click on the Engage icon) to engage the tip (the motor value located at the bottom of the monitor displays the number of microns the motor has moved down from its original position).
- 2 Wait until the tip engages the surface.

If it fails to engage because the tip is too far from the wafer:

- a. Go to Motor/Withdraw then go to Stage/Focus Surface.
- b. Using the roller, manually move the SPM 50-100 um more negative.
- c. Repeat "Engage" until motor no longer fails.

If it fails to engage because the tip is too close to the wafer:

- a. Go to Motor/Withdraw 2-3 times.
- b. Using the roller, manually move the SPM 50-100 um more positive.

- c. Repeat "Engage" until motor no longer fails.
- 3 Once contact with the wafer surface occurs, go to View/Scope Mode (This will show the Scope Trace on the right monitor).

Adjusting scan parameters

- 1 Go to View/Scope Mode (or click on the Scope Mode icon).
- 2 Check to see if Trace and Retrace are tracking each other well (i.e. look similar).
If they are tracking, the lines should look the same, but they will not necessarily overlap each other, either horizontally or vertically.

IF tracking well (tip is scanning on the sample surface):

- a. Click on Setpoint and use right arrow key to gradually increase the Setpoint value, until the tip lifts off the surface (at this point the Trace and Retrace will no longer track each other).
- b. Next, decrease the Setpoint with the left arrow key until the Trace and Retrace follow each other again.
- c. Decrease the Setpoint 1-2 arrow clicks more to ensure that the tip will continue to track the surface.
- d. Go to View/Image Mode (or click on the Image Mode icon) to view the image.

IF not tracking well:

- a. Adjust the Scan Rate, Gains, and/or Setpoint to improve the Tracking.

- b. For scan sizes of 1-3um try scanning at 2Hz; for 5-10um, try 1Hz; and for large scans, try 1.0-0.5Hz.

Setting desired scan size, scan angle and offsets

- 1 Once the scan parameters are optimized, scan size and other features can be adjusted for capturing images for analysis.
- 2 When changing the scan size value, keep in mind that the scan rate will need to be lowered for larger scan sizes.

Capturing the image

- 1 Go to View/Image Mode to view the surface image on the right Monitor.
- 2 Make sure the hood is closed while capturing the image.
- 3 Capture the image by going to Capture/Capture File Name and name the file.
- 4 Then, go to Capture/Capture (this will save your captured image).

Shutdown

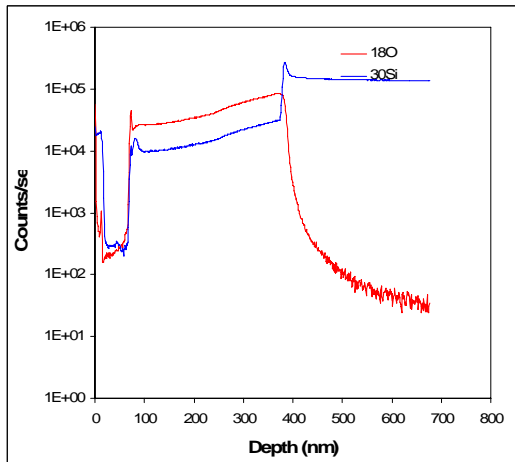
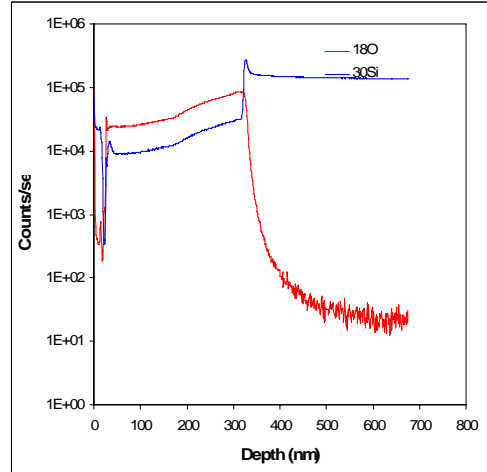
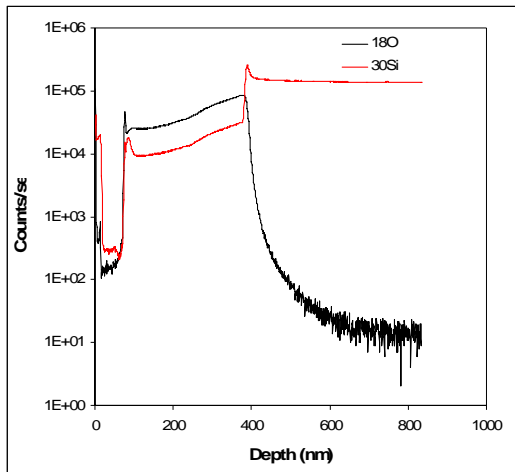
- 1 Go to Motor/Withdraw 4-5 times.
- 2 This takes the cantilever off the surface.
- 3 Visually check the distance of the tip to the wafer surface to ensure that there is adequate space to prevent the tip from crashing.
- 4 Go to Stage/Load New Sample, then click OK.
- 5 This will move the SPM and wafer chuck to the unload position.
- 6 Turn off the vacuum.

- 7 Carefully unload your wafer with tweezers.
- 8 Remember to: unload your tip and make sure the hood is closed.
- 9 Disable the AFM.

APPENDIX C

SIMS Measurements

Other samples characterized by the SIMS, for the first two samples, silicon was deposited for 60 seconds and the third sample had silicon deposited for 30 seconds. The deposited silicon thicknesses were estimated to be approximately 12.7, 13.8 and 5.7 nm respectively.



APPENDIX D

AFM Radius Measurements

30 Seconds Deposition

600°C	650°C	700°C	750°C	800°C	850°C	900°C
18.7	17.8	23.29	33.89	39.16	37.58	49.82
15.24	21.04	32.75	33.26	29.38	40.33	47.7
16.85	21.75	27.28	33.13	41.12	37.01	46.05
15.54	19	28.75	38.66	36.13	43.83	49.84
19.94	19.6	25.24	27.7	36.77	45.48	50.9
16.41	16.71	33.56	30.57	47.43	37.13	40.24
19.34	16.63	33.11	34.29	37.29	44.84	47.12
16.26	20.78	29.49	31.21	37.62	45.1	42.73
15.24	17.78	28.78	35.44	37.16	36.61	49.45
16.14	20.33	25.13	36.05	42.85	42.73	43.62
14.56	18.35	29.55	25.45	42.23	40.42	44.44
18.25	19.48	26.58	29.95	46.51	45.75	56.46
18.25	18.21	29.04	36.98	38.67	43.8	39.77
16.87	17.8	24.37	30.53	41.07	36.52	46.53
19.89	18.97	25.83	26.29	40.38	46.75	46.4
14.67	17.8	28.22	29.95	37.65	40.33	48.96
16.53	15.6	24.37	31.13	37.22	43.34	42.93
14.58	16.41	26.3	31.7	35.26	42.29	41.87
15.55	19	33.11	34.41	42.92	44.85	46.02
18.04	19	25.17	31.46	41.26	39.52	38.83
14.67	18.48	24.37	33.83	36.11	43.1	45.19
13.63	21.1	27.38	27.1	35.08	41.22	40.8
14.35	17.04	32.05	31.95	38.79	37.77	50.44
18.7	19	26.33	31.46	41.07	44.73	37.9
13.16	22.02	24.68	28.55	38.01	40.12	49
14.78	20.46	27.28	32.13	39.38	41	38.43
17.88	19.87	29.3	32.91	42.92	41.19	47.84
15.82	20.71	26.58	29.97	41.56	40.42	38.39
14.35	20.46	24.22	29.51	35.92	40.72	43.93
16.72	19.49	26.15	37.57	37.79	40.29	47.75
14.78	22.02	28.88	27.37	41.13	42.84	45.16
17.57	16.71	33.08	37.13	37.42	44.41	41.03
17.8	20.71	22.07	28.76	41.07	40.72	39.26
18	17.46	23.31	31.13	41.64	41.7	40.45
13.6	17.23	34.31	33.78	41.14	43.25	51.54
17.57	23.85	24.37	31.67	44.13	41.66	38.43
16	21.81	28.88	29.95	37.65	41.47	42.73

17.52	16	25.57	31.45	44.06	40.28	41.38
16.76	20.46	20.35	33.13	45.73	41.87	46.85
18.52	21.4	30.4	27.47	45.52	41.75	43.77

60 Seconds Deposition

600°C	650°C	700°C	800°C	850°C	900°C
18.23	20.64	31.96	43.62	47.05	55.58
19.75	24	26.87	35.19	41.38	63.15
16.01	24	35.73	42.27	45.34	58.24
17	21.46	29.67	42.77	44.62	65.21
17.47	22.4	38.57	40.94	44.94	68.65
19.67	27.35	34.73	40.94	42.39	63.62
18.66	18.52	29.67	37.81	42.39	56.32
16.8	18.27	35.73	39.02	38.39	54.81
21	19.71	32.77	37.06	36.17	55.66
16.56	21.67	30.55	32.57	41.82	63.15
20.72	23.75	29.67	39.91	35.55	63.57
18.42	27.9	36.22	44.22	46.12	47.81
18.91	23.65	29.37	42.77	35.6	56.77
23.2	20.36	34.73	43.62	45.83	62.35
20.31	20.24	29.12	37.1	44.08	51.39
18.17	22.56	30.98	42.45	49.64	65.5
19.41	20.41	35.85	37.81	40.44	47.81
16.33	21.56	31.96	41.5	48.88	47.03
14.3	26.5	29.67	42.31	49.62	59.57
20.31	19.19	27.36	40.98	47.93	55.77
15.1	26.54	27.36	30.57	39.25	47.03
17.03	17.17	27.36	41	40.25	60
17.4	24	38.69	41.7	44.71	64.2
14.86	20.41	28	40.36	38.47	63.2
17.27	19.72	26.87	38.66	50.22	58.22
18.65	21.3	34.6	41.04	46.21	58.24
20.16	19.72	31.54	35.71	38.23	51.31
13.59	20.36	32.1	35.74	37.67	59.47
19.42	21.08	28	35.19	41.79	51.31
20.72	19.58	34.73	40.34	39.76	52.22
20.1	24	34.73	44.34	39.23	55.58
17.4	22.76	27.36	44.65	48.24	47.03
16.97	19.96	31.54	41.01	38.38	51.39
17.23	20.64	33.17	37.83	50.24	48.8
15.15	21.13	32.1	39.86	41.76	59.74
17.68	21.72	26.7	41.54	37.06	57.56
13.33	22.7	32.1	44.48	48	46.06
17.43	16.96	27.36	35.19	39.68	52.22
17.4	20.36	31.54	34.17	47.24	57.57
14.18	24.7	32.1	38.18	50.31	50.11

Temperature and Average Radii Data

Temperature °C	30 seconds	60 seconds
600	16.4758	17.8075
650	19.208	21.7237
700	27.487	31.4782
750	31.72175	--
800	39.855	39.6605
850	41.614	43.122
900	44.7488	56.3305

REFERENCES

1. en.wikipedia.org/wiki/Silicon.
2. <http://phasela.unl.edu/~xczeng/si-highlight.pdf>.
3. L. J. De Jongh, Electronic Properties of Metalcluster Compounds: Nanophase Materials from Chemical Synthesis, Nanophase Materials. 1994. pp 349.
4. G. Schmid, Nanoparticles: From Theory to Application. 2004 WILEY-VCH Verlag GmbH & Co. KGaA, Weinheim. pp. 4-5.
5. M. A. H. Khalafalla, Z. A. K. Durrani, H. Mizuta, Coherent states in a coupled quantum dot nanocrystalline silicon transistor. 2004 Applied Physics Letters, Vol. 85 pp 2262 – 2264.
6. Z. Yaniv, Nanoscience and Nanotechnology: two new exciting fields for future display applications, Applied Nanotech, Inc – Austin, Texas.
7. B. J. Hinds, T. Yamanaka, S. Oda, Emission lifetime of polarizable charge stored in nano-crystalline Si based single-electron memory. 2001 Journal of Applied Physics, Vol. 90 pp 6402 – 6408.
8. A. Bapat, C. Anderson, C. R. Perrey, C.B. Carter, A. S. Campbell, and K. Uwe, Plasma synthesis of single crystal silicon nanoparticles for novel electronic device applications. 2004. pp 4-6, 17-18.9. M. H. Neyfeh, N. Barry, O. Therrien, O.
9. M. H. Nayfeh, N. Barry, O. Therrien, O. Akcakir, E. Gratton, and G. Belomoin, Stimulated blue emission in reconstituted films of ultrasmall silicon nanoparticles. 2001 Applied Physics Letters, Vol. 78 Number 8 pp 1131-1133.
10. R. K. Baldwin, K. A. Pettigrew, J. C. Garno, P. P. Power, G. Liu, and S. M. Kauzlarich, Room temperature solution synthesis of alkyl-capped tetrahedral shaped silicon nanocrystals. 2002 Journal of the American Chemical Society, Vol. 124 Number 7 pp 1150-1151.
11. G. Ledoux, J. Gong, F. Huisken, O. Guillois, C. Reynaud, Photoluminescence of size-separated silicon nanocrystals: confirmation of quantum confinement. 2002 Applied Physics Letters, Vol. 80 Number 25 pp 4834-4836.

12. P. E. Batson, J. R. Heath, Electron energy loss Spectroscopy of single silicon nanocrystals: the conduction band. 1999 Physical Review Letters, Vol. 71 Number 6 pp 911-914.
13. E. Borsella, M. Falconieri, S. Botti, F. Bignoli, L. Costa, S. Grandi, L. Sangaletti, B. Allieri, and L. Dpero, 2001 Material Science & Engineering, B: Solid-State Materials for Advanced Technology Vol. B79 Number 1 pp 55-62.
14. S. Oda, 1997 Adv. Colloid Interfac. Sci. 71-72 pp 31-37.
15. C. R. Gorla, S. Liang, G. S. Tompa, W. E. Mayo, and Y. Lu, 1997 J. Vacuum Science and Technology Vol. A 15 pp 860.
16. G. Viera, S. Heut, M. Mikikian, and L. Boufendi, 2002 Thin Solid Films Vol. 403 pp 467-470.
17. G. Viera, M. Mikikian, E. Bertran, P. R. I. Cabarrocas, and L. Boufendi, 2002 Journal of Applied Physics Vol. 92 Number 8. pp 4684-4694.
18. X. Du, M. Takeguchi, M. Tanaka, and K. Furuya, Formation of crystalline Si nanodots in SiO₂ films by electron irradiation. 2003 Applied Physics Letters Vol. 82 Number 7. pp 1108-1110.
19. S. Seo, J. Lee, and J. H. Shin, The thermo-optic effect of Si nanocrystals in silicon-rich silicon oxide thin films. 2004 Applied Physics Letters Vol. 85 Number 13. pp 2526-2528.
20. B. Legrand, V. Agache, J. P. Nys, V. Senez, D. Stienvenard, Formation of silicon islands on a silicon on insulator substrate upon thermal annealing. 2000 Applied Physics Letters Vol. 76 Number 22. pp 3271-3273.
21. M. Ohring, The Materials Science of Thin Films. Harcourt Brace Jovanovich, Publishers, 1992, pp. 137.
22. Thin film deposition solutions – RF Ion Source RF50, version 2.1; Oxford Applied Research.
23. A. Benninghoven, G. F. Rudenauer, W. H. Werner, Secondary Ion Mass Spectrometry. A Wiley-Interscience Publication, 1987, pp. 1-4.
24. http://www.nrel.gov/pv/measurements/static_time_flight.html.
25. http://www.nrel.gov/pv/measurements/dynamic_secondary_ion.html.

26. G. R. Wilson, A. F. Stevie, W. C. Magee, Secondary Ion Mass Spectrometry – A practical handbook for depth profiling and bulk impurity analysis. A Wiley-Interscience Publication, 1989, pp. I-2 – I-3, 1.5-1.
27. SPM Training Notebook; (Copyright 2003 Veeco Instruments Inc); pp 8-13.
28. <http://chemistry.jcu.edu/mwaner/research/AFM/>.
29. <http://www.chembio.uoguelph.ca/educmat/chm729/afm/details.htm#contact>.
30. http://vpd.ms.northwestern.edu/teaching/AFM_MSc_190_lab.pdf.
31. R.W. Carpick, M. Salmeron, Scratching the surface: Fundamental investigations of tribology with atomic force microscopy. 1997 Chemical Reviews Vol. 97 Number 4. pp 1167.
32. microlab.berkeley.edu/labmanual/chap5/5.33.html.
33. <http://www.rpi.edu/dept/cie/mncr/coserta.html>.
34. C. Suryanarayana, M. G. Norton, X-Ray Diffraction-A practical approach. Plenum Publishing Corporation, 1998, pp. 1, 14.
35. <http://www.mrl.ucsb.edu/mrl/centralfacilities/xray/xray-basics/index.html#x1>.
36. http://www.mtec.or.th/th/labs/xrd&xrf/xrd_tech.html.
37. Y. Wakayama, T. Takashi, T. Shun-ichiro, Formation of Si islands from amorphous thin films upon thermal annealing. 1999, Applied Physics Letters Vol. 85, Number 12. pp 8492-8494.

VITA

Benedict Anyamesem-Mensah was born in Kumasi, Ghana, on May 25, 1978, the son of Margaret Kobi and Paul Anyamesem-Mensah. After completing his work at Opoku Ware Secondary School, Kumasi in 1996, he entered Kwame Nkrumah University of Science and Technology, Kumasi, Ghana. He received the degree of Bachelor of Science for Physics in spring of 2002. In the spring of 2005 he entered the Graduate College at Texas State University-San Marcos to pursue his Master of Science degree. During his graduate studies, he was employed as an instructional assistant and worked as quality engineer intern at International Sematech, Austin.

Upon completion of the degree of Master of Science for Physics, Benedict will begin his doctoral studies in Material Science and Engineering at University of North Texas, Denton.

Permanent Address: 327 West Woods St. Apt. 501

San Marcos, Texas 78666

This thesis was typed by Benedict A. Mensah.